JGR Atmospheres

RESEARCH ARTICLE
10.1029/2026JD046770

Trace Elements in Total Atmospheric Deposition Directly Measured Over the Caribbean Region: Natural Versus Anthropogenic Sources and Geographic Origin

Yangjunjie Xu-Yang[1,2], Rémi Losno[1], Céline Dessert[1], Fabrice Monna[3], Damien Guinoiseau[4], Antoine Cogez[1], and Carmela Chateau-Smith[5]

[1]Institut de Physique du Globe de Paris, CNRS UMR 7154, Université Paris Cité, Paris, France, [2]Laboratoire des Sciences du Climat et de l'Environnement (LSCE), CEA, CNRS, UVSQ, Université Paris-Saclay, Gif-sur-Yvette, France, [3]Université Bourgogne Europe, UMR CNRS 6298, ARTEHIS, Dijon, France, [4]Université Paris-Saclay, CNRS, GEOPS, Orsay, France, [5]Université Bourgogne Europe, CNRS, Biogéosciences UMR 6282, Centre Pluridisciplinaire Textes et Cultures, UR 4178, Dijon, France

Abstract Dust, sea salt, and anthropogenic and biogenic particles in total atmospheric deposition are sources of essential elements that can significantly impact biogeochemical cycles in the Atlantic Ocean and in islands of the Caribbean region. This unique 41-month data set records direct sampling of total atmospheric deposition from March 2015 to August 2018 in Guadeloupe (North Tropical Atlantic Ocean). It quantifies the total atmospheric deposition fluxes of 33 trace elements. Results on deposition samples for Sr and Nd isotopic signatures are consistent with previous studies conducted in the Caribbean region based on aerosol samples, confirming that trans-Atlantic Saharan dust originated predominantly in the Libya-Algeria-Mali region of North Africa. The REE composition is stable for the majority of samples, though some slight inter-annual variation was observed. Samples collected in 2016 present slightly different REE patterns compared to those collected in 2015, 2017, and 2018. A large fraction of some trace elements (Se, Sb, Cu, Mo, As, and Pb) may come from biogenic sources or from atmospheric pollution occurring at the global level. Lead isotope ratios reveal a mixture of transatlantic dust from the Libya-Algeria-Mali region, and anthropogenic sources with no clearly defined region of origin. This result highlights the need for updated reviews of aerosol lead isotopic signatures worldwide. Backward trajectory analysis suggests that atmospheric pollution from North America and Europe may be a significant source of Sb, whereas biogenic gas from the Sargasso Sea may contribute to high levels of Se.

Plain Language Summary Major and trace elements from atmospheric deposition provide essential nutrients for tropical islands in the Caribbean region. To evaluate their impact on the biogeochemical cycle of this region, the atmospheric deposition fluxes of these elements must be quantified. We therefore investigated the deposition fluxes of 33 trace elements in Guadeloupe from 2015 to 2018. Lead isotope ratios show a combination of anthropogenic sources with unclear origins and transatlantic dust from desert regions in North Africa. Neodymium and strontium isotopic signatures, and rare earth element composition are used to identify the geographic origin of crustal elements more precisely. We concluded that the major sources of these elements are dust from North African desert regions (Libya-Algeria-Mali), sea salt from the Atlantic Ocean, aerosol particles from human activities (e.g., atmospheric pollution at the global level), and terrestrial and marine biological sources.

Key Points:

- Total trace element atmospheric deposition flux is directly measured during 41 months (March 2015–August 2018) in Guadeloupe Island, Caribbean
- Isotope tracers ($^{143}Nd/^{144}Nd$; $^{87}Sr/^{86}Sr$) confirm that the Libya-Algeria-Mali region is the major source of dust transported to Guadeloupe
- For some trace elements (Sb, Cu, Mo, Se, As, and Pb), a large fraction may be associated with atmospheric pollution and biogenic emissions

Correspondence to:
Y. Xu-Yang,
xuyangjunjie@gmail.com

Citation:
Xu-Yang, Y., Losno, R., Dessert, C., Monna, F., Guinoiseau, D., Cogez, A., & Chateau-Smith, C. (2026). Trace elements in total atmospheric deposition directly measured over the Caribbean region: Natural versus anthropogenic sources and geographic origin. *Journal of Geophysical Research: Atmospheres*, *131*, e2026JD046770. https://doi.org/10.1029/2026JD046770

Received 26 FEB 2026
Accepted 29 JUL 2026

Author Contributions:
Conceptualization: Yangjunjie Xu-Yang, Rémi Losno, Céline Dessert, Fabrice Monna
Data curation: Yangjunjie Xu-Yang, Rémi Losno, Damien Guinoiseau, Antoine Cogez
Formal analysis: Yangjunjie Xu-Yang, Rémi Losno, Fabrice Monna, Damien Guinoiseau
Funding acquisition: Rémi Losno, Céline Dessert
Investigation: Yangjunjie Xu-Yang, Rémi Losno, Fabrice Monna

1. Introduction

Atmospheric aerosols are solid or liquid particles suspended in the atmosphere, either of natural origin (desert dust, sea salt, primary biogenic particles, wildfires, and volcanic emissions) or from anthropogenic sources (e.g., industrial and agricultural activities, transport emissions, and incineration) (Lu et al., 2024; Mahowald et al., 2011; Rathod et al., 2024; Vet et al., 2014; Wong et al., 2021). Atmospheric aerosols can modify the atmospheric radiation budget and cloud features, thus influencing climate (Mahowald et al., 2011). They can participate in photochemical reactions and also affect public health (Mahowald et al., 2011). Once they fall to the ground or into the ocean through atmospheric deposition, aerosol particles can provide micro-nutrients and participate in global biogeochemical cycles (Chadwick et al., 1999; Jickells et al., 2005; Mahowald et al., 2011, 2014; Okin et al., 2011).

Methodology: Yangjunjie Xu-Yang, Rémi Losno, Céline Dessert, Fabrice Monna, Damien Guinoiseau, Antoine Cogez
Project administration: Rémi Losno, Céline Dessert
Resources: Yangjunjie Xu-Yang, Rémi Losno
Software: Yangjunjie Xu-Yang, Rémi Losno, Fabrice Monna
Supervision: Yangjunjie Xu-Yang, Rémi Losno, Céline Dessert
Validation: Yangjunjie Xu-Yang, Rémi Losno, Céline Dessert, Fabrice Monna, Damien Guinoiseau
Visualization: Yangjunjie Xu-Yang, Rémi Losno
Writing – original draft: Yangjunjie Xu-Yang, Rémi Losno
Writing – review & editing: Yangjunjie Xu-Yang, Rémi Losno, Céline Dessert, Fabrice Monna, Damien Guinoiseau, Carmela Chateau-Smith

Sea salt and trans-Atlantic Saharan dust are the major components of total atmospheric deposition in the Amazon Basin, the Caribbean region, and the Atlantic Ocean (e.g., Dessert et al., 2020; Pett-Ridge et al., 2009; Pourmand et al., 2014; Vet et al., 2014; Xu-Yang et al., 2022; H. Yu et al., 2015). This process supplies essential nutrients to tropical forests in the Amazon Basin (e.g., H. Yu et al., 2015) and in the Caribbean region (e.g., Abouchami et al., 2013; Dessert et al., 2020; McClintock et al., 2015, 2019; Pett-Ridge et al., 2009; Xu-Yang et al., 2022). Dessert et al. (2020) have characterized the impact of Saharan dust on the biogeochemical balance of nutrients in Guadeloupean ecosystems in the Caribbean region. Analyses of soil profiles and plants show that, in the northern part of Guadeloupe, the ecosystem is sustained by a small, near-surface nutrient pool disconnected from the deep volcanic bedrock (Dessert et al., 2020). In this case, the forest community is sustained by efficient nutrient recycling. As a consequence, Saharan dust and sea salt play a significant role in maintaining ecosystem productivity in Guadeloupe over long timescales (Clergue et al., 2015; Dessert et al., 2020).

Micro- and macro-nutrients from atmospheric deposition play a similar role in the marine ecosystem of the Atlantic Ocean by supplying nitrogen (N), phosphorus (P), silica (SiO_2), and iron (Fe) to regulate phytoplankton growth (Browning & Moore, 2023; Jickells et al., 2005; Moore et al., 2013; Okin et al., 2011; Pabortsava et al., 2017; Schlosser et al., 2014). Mineral particles acting as ballast can increase the sinking rate of particulate organic matter, thus enhancing carbon export and deep sequestration of nutrients from the remote surface ocean (e.g., Guerreiro et al., 2017; Guerreiro et al., 2023; Okin et al., 2011; Van Der Jagt et al., 2018).

The abundance and bio-availability of nutrient elements in North African dust can vary greatly, in relation to the region of emission (Guinoiseau et al., 2022; Moreno et al., 2006; Scheuvens et al., 2013). Identifying dust sources and composition is important to assess the role of dust deposition in tropical ecosystems and in surface sea water biogeochemistry (Hudson-Edwards et al., 2014; Moore et al., 2013). Six potential source areas (PSAs) in North Africa are defined in a recent study combining the geochemical fingerprint of fine surface soil ($<20\,\mu m$) with the subdivision of North African geological provinces (Guinoiseau et al., 2022). The six PSA are: (a) Libya-Algeria-Mali [PSA (LAM)], (b) Libya-Egypt [PSA (LE)], (c) Bodélé Depression [PSA (BD)], (d) Mali Center [PSA (MC)], (e) West African Coast [PSA (WAC)] and (f) Mauritania [PSA (Ma)]. That study (Guinoiseau et al., 2022) also identified PSA (LAM) and PSA (WAC) as the major geological origin of dust for the Caribbean region.

The chemical composition of biogenic aerosols varies greatly (e.g., Mao et al., 2021; Martin et al., 2010). Atmospheric deposition of biogenic particles can be a major source of elements such as phosphorus and selenium. Biogenic particles containing microorganisms and aerosols from biomass burning (both of African origin) could be major sources of phosphorus deposition in the reception regions, including the Mediterranean Sea, Amazon Basin, tropical Atlantic Ocean, and Southern Ocean (Barkley et al., 2019; Violaki et al., 2025). Atmospheric deposition of biogenic selenium, produced through biomethylation (Breuninger, Tolu, Aemisegger, et al., 2024; Breuninger, Tolu, Thurnherr, et al., 2024; Schlesinger et al., 2022), is a substantial source of dietary selenium in food chains (Feinberg, Maliki, et al., 2020; Feinberg, Stenke, et al., 2020), and is also important for agricultural soil (Combs, 2001).

In recent years, deposition of major and trace elements (e.g., Fe, Mn, and Mo) originating from atmospheric pollution associated with human activities has been shown to perturb the atmospheric cycle of trace elements and to impact terrestrial and oceanic ecosystems (Lu et al., 2024; Rathod et al., 2020, 2024; Wong et al., 2021). Molybdenum is considered to be the most common constraint on nitrogen fixation across terrestrial ecosystems (Barron et al., 2009; Rousk et al., 2017; Wurzburger et al., 2012). Anthropogenic activities, such as combustion, vehicular emissions, and agricultural dust, contribute 40%–75% of the annual atmospheric molybdenum emissions, serving as a substantial source of atmospheric molybdenum deposition in the Caribbean and a primary source in the Amazon Basin and over North America (Wong et al., 2021). Antimony is a new emergent hazardous environmental pollutant transported by the atmosphere at global scale. It has been detected worldwide, in Alpine snow and ice cores (Barbante et al., 2004; Van De Velde et al., 1999), and even in Antarctic ice cores (Hur et al., 2013; Krachler et al., 2005, 2008). More studies are required to fully document the atmospheric deposition of antimony and its spatial and temporal variation.

According to the Intergovernmental Panel on Climate Change (IPCC), despite advances in modeling and satellite analysis, high uncertainties subsist in predicting modern dust cycles and their impact due to anthropogenic-induced changes in aerosol concentrations (IPCC, 2023). Sea-salt emissions and deposition also exhibit significant uncertainties on the enrichment of trace elements in the sea surface microlayer from which the sea-salt aerosols are emitted (e.g., Marsay et al., 2022; Weisel et al., 1984). Global model predictions of sea-salt

emissions are frequently limited by observations obtained at coastal monitoring sites, where shoreline wave breaking significantly increases the coastal sea spray aerosol population, thereby amplifying the uncertainties associated with this crucial aerosol component (Zhou et al., 2025). In terms of biogenic and anthropogenic trace elements, direct measurements of atmospheric aerosol concentration and deposition are sparse at the global scale, in general, and in the Caribbean region, in particular. Most studies are based on the analysis of aerosol samples, conducted over a short period of time or using discrete events (e.g., Aarons et al., 2013; Bozlaker et al., 2018; Grousset et al., 1988; Kumar et al., 2014, 2018; Pourmand et al., 2014; Van Der Does et al., 2018; Witt et al., 2006), or based on marine sediment traps (e.g., Van Der Does et al., 2018). Some studies have reported only a few major elements (e.g., Heartsill-Scalley et al., 2007; McClintock et al., 2019; Prospero et al., 2010); others were conducted decades ago (e.g., Cutter, 1993; Cutter & Church, 1986), and should therefore be updated, as anthropogenic forcing has accelerated since then (Feinberg, Maliki, et al., 2020; Feinberg, Stenke, et al., 2020; Lu et al., 2024; Mahowald et al., 2025; Rathod et al., 2020, 2024; Wong et al., 2021).

At the global scale, long-term, continuous, high-frequency sampling in remote regions is required to accurately evaluate the atmospheric deposition of major and trace elements, which can then be used to test and adjust the global models (Mahowald et al., 2025; Wong et al., 2021). Isotope records on past and present deposition samples can be used to constrain the geological origin and strength of dust emissions (Guinoiseau et al., 2022; Rousseau et al., 2025; Skonieczny et al., 2013). At the regional scale, these measurements are crucial to comprehend nutrient input and output balance in the high-weathering tropical forest context of the Caribbean region, which will enhance understanding of the interaction between the region's tropical ecosystem and global biogeochemical cycles (Clergue et al., 2015; Dessert et al., 2020; Fries et al., 2019). In previous studies (Xu-Yang et al., 2022), the atmospheric deposition fluxes of Saharan dust, sea salt, and other major elements are quantified and their deposition mechanism (total vs. dry) is studied in comparison with the Community Atmosphere Model (CAM6) (Xu-Yang et al., 2025).

The aims of the present study are: (a) to create an exceptional database for isotopes ($^{143}Nd/^{144}Nd$; $^{87}Sr/^{86}Sr$; $^{206}Pb/^{207}Pb$; $^{208}Pb/^{207}Pb$) and Rare Earth Elements (REEs) in total atmospheric deposition, which are of particular interest in tracing the specific origin of trans-Atlantic Saharan dust; (b) to measure the total atmospheric deposition fluxes of trace elements, particularly those linked to poorly defined anthropogenic and biogenic emissions; (c) to identify the origin of these trace elements by combining backward trajectory analysis, enrichment factors, and data from previous field and model studies. To achieve these goals, total atmospheric deposition was collected continuously during 41 months, from March 2015 to August 2018, providing one of the most complete datasets of trace elemental and isotopic compositions over the longest time series in atmospheric deposition from the Caribbean region.

2. Material and Method

2.1. Deposition Sample Collection

The sampling site is located in Guadeloupe in the Caribbean region; it is often close to the center of the trans-Atlantic Saharan dust plume, as shown in Figure 1. Total atmospheric depositions were sampled continuously during an integration period ranging from 6 to 14 days (depending on weather conditions and local logistic support) at the remote site of OVSG (Observatoire Volcanologique et Sismologique de Guadeloupe, Gourbeyre, Guadeloupe, 15°58′50″N, 61°42′13″W, 411 m asl; Figure 1). The total atmospheric deposition was sampled with a 12 cm diameter funnel made of Teflon™, attached to a clean 1 L polypropylene bottle pre-loaded with 50 ml of ultra-pure 3% v:v HCl aqueous solution and left open to total atmospheric deposition. The sampling system was fixed 2 m above the roof of a building and approximately 12 m above ground level. Each time a sample was renewed, 50 ml of a 3% v:v HCl water solution was poured into the funnel to collect the residual and to rinse it, and the bottle was replaced by a new one. Each sample was then weighed and completely evaporated under ultra-filtered airflow at 85°C as described in Xu-Yang et al. (2022). Dry deposition on the funnel surface may undergo wind-driven remobilization, representing about 6%–13% of total deposition (Izquierdo & Avila, 2012). However, in Guadeloupe, high rainfall frequency and persistent humidity likely limit this effect. Variability between sampling methods or duplicates is generally <15% for major elements (Heimburger et al., 2012; Izquierdo & Avila, 2012), suggesting a minor impact. Continuous sampling started on 2 March 2015, and ended on 3 August 2018. One hundred forty-two samples were successfully collected and analyzed. The daily precipitation rate of the OVSG site during the sampling period varied between 0 and 300 $mm \cdot day^{-1}$, with a median

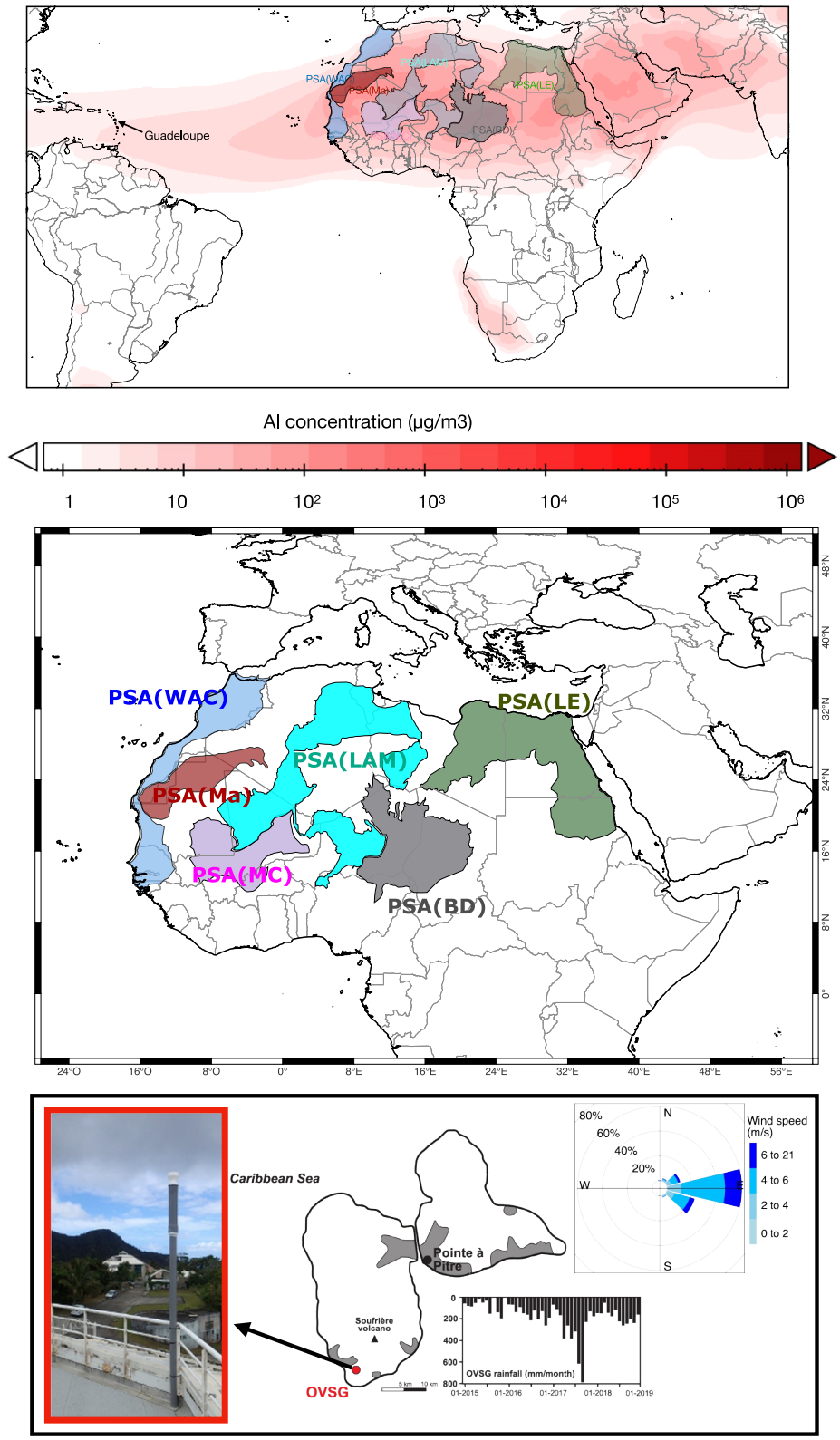

Figure 1.

value of 2 mm·day^{-1}. During the sampling period, the average deposition mass flux was 17.4 g·m^{-2}·yr^{-1} for sea salt and 11.2 g·m^{-2}·yr^{-1} for Saharan dust, with no noticeable inter-annual variation (for further details, see Xu-Yang et al. [2022]).

2.2. Sample Digestion and Chemical Analysis of Trace and Major Elements

Samples were processed in clean rooms using Milli-Q™ ultra-pure water and sub-boiled ultra-pure acids. First, 5 ml of a mixture of HCl:HF acids (3:1 v:v) was added to each evaporated sampling bottle and heated for 48 hr at 70°C to dissolve mineral residues. After cooling, contents were transferred into a 60 ml Teflon™ bottle, rinsed with 20 ml of Milli-Q™ ultra-pure water and 3 ml of 67% nitric acid to recover the remaining material. Combined solutions were evaporated through staged heating (99°C for 10 hr and then at 115°C until complete evaporation), removing acids and silica, while concentrated nitric acid completed digestion of organic matter at the end of the evaporation process. Residues were dissolved in diluted nitric acid, transferred to clean bottles, and diluted to around 100 ml with Milli-Q™ ultra-pure water. Major and minor elements (Al, Ba, Ca, Fe, Mg, Mn, P, S, Sc, Sr, Ti, and Zn) were measured using an ARCOS (Spectro-Ametek) ICP-AES, equipped either with a CETAC ultrasonic nebulizer or with a concentric nebulizer coupled to a cyclonic chamber (see Xu-Yang et al. (2022) and Xu-Yang et al. (2025) for discussion of these elements). Two elements (Na and K) were measured using a flame photometer (Cole Parmer 360) with an external calibration between 0 and 50 µg·ml^{-1} (Xu-Yang et al., 2022). Trace elements (Be, V, Cr, Co, Ni, Cu, As, Se, Rb, Mo, Sb, Tl, Pb, and U) and rare earth elements (REEs) were measured using a Element 2 Thermo Scientific™(HR-ICP-MS), equipped with a concentric micro-nebulizer coupled to a cyclonic chamber (see Xu-Yang et al. [2025] for discussion of these elements). High-resolution analysis avoids polyatomic interference for elements lighter than arsenic, and also for REEs (Heimburger, Tharaud, et al., 2013). The elemental analysis procedure is detailed in Xu-Yang et al. (2022) and Xu-Yang et al. (2025). Limits of detection (calculated as three times the standard deviation of field blanks) and recovery rates of measurement are listed in Tables A1 and A2.

2.3. Analysis of Lead Isotope Ratios

Lead isotopes (^{206}Pb, ^{207}Pb, and ^{208}Pb) were analyzed with the Element 2 Thermo Scientific™(HR-ICP-MS). Before measurement, concentrations of ^{208}Pb were adjusted to an ion flux in the [200,000–800,000] cps range, to achieve optimal precision in counting without losing the linearity of the detector response due to excessive flux. Nevertheless, 27 deposition samples could not be measured for ^{208}Pb because the signal was outside the targeted range. The appropriate correction factor [ranging from 1.0000 to 1.0050 for ^{207}Pb/^{206}Pb; from 0.9829 to 1.0025 for ^{208}Pb/^{206}Pb, and from 0.9780 to 1.0024 for ^{208}Pb/^{207}Pb] was applied to raw measured ratios. This factor was obtained through repeated measurements of NBS 981 lead isotope standard every 10 samples and verified by STM-1 geostandard (Table 1).

2.4. Analysis of Neodymium and Strontium Isotopic Signatures (εNd and ^{87}Sr/^{86}Sr)

The purification and analysis of Nd followed the same procedure as that used by Cogez et al. (2015). Briefly, the first step purified REEs and actinides using TRU-spec® resin in HNO_3 2 mol.L^{-1}. The second step was the purification of Nd using Ln-spec® resin in HCl 0.25 mol.L^{-1}. The ^{143}Nd/^{144}Nd isotopic ratio was determined by mass spectrometry, using the MC-ICP-MS Neptune (Thermo Scientific™). Results were corrected for interference with ^{144}Sm, and for instrumental mass discrimination with the exponential discrimination law, using the stable ratio ^{146}Nd/^{144}Nd = 0.72190. To evaluate measurement accuracy, samples were bracketed with Nd NIST standard (NISTSRM3135a), for which a ratio of 0.511418 has been determined by Caro et al. (2006) using thermo-ionization mass spectrometry. The Nd NIST standard was analyzed every four samples to correct for instrumental drift. Only samples containing at least 50 ng of Nd were selected for Nd isotope analysis. After

Figure 1. Sampling site in Guadeloupe and Potential Source Areas (PSAs) of trans-Atlantic dust in North Africa. (Upper panel) Location of Guadeloupe showing modeled surface aerosol Al concentration between 2013 and 2015 in PM_{10} (Mahowald et al., 2025). The Guadeloupe Islands are inside the transatlantic dust plume. The location of Guadeloupe is indicated by an arrow. (Middle panel) Detailed definition and location of the six PSAs as defined by Guinoiseau et al. (2022), based on geochemical fingerprint studies and subdivision of North African geological provinces. PSA (LAM), Libya-Algeria-Mali; PSA (WAC), West African Coast; PSA (MC), Mali Center; PSA (BD), Bodélé Dépression; and PSA (LE), Libya-Egypt. (Lower panel) sampling site in Guadeloupe, on the roof of the OVSG building; gray zones show urban areas; monthly rainfall data (Xu-Yang et al., 2022); windrose shows frequency of count by wind direction from east to west (ERA5 hourly time-series data for sampling site between 2012 and 2025).

Table 1
Comparison of Pb Isotope Ratios Measured in One STM-1 in the Present Study With Results Obtained by Weis et al. (2006)

Ratios	Measured	Published
$^{207}Pb/^{206}Pb$	0.7994 ± 0.0009	0.801 ± 0.001
$^{208}Pb/^{206}Pb$	2.000 ± 0.002	2.008 ± 0.003
$^{208}Pb/^{207}Pb$	2.502 ± 0.004	2.507 ± 0.002

sequential column separation, the final solution (v = 1 ml) was injected into the MC-ICP-MS. The εNd notation, which represents a relative difference to the CHondritic Uniform Reservoir (CHUR) value of 0.512638 (Jacobsen & Wasserburg, 1984) calculated using Equation 1, was adopted for convenience.

$$\varepsilon Nd = \left[\frac{\left(^{143}Nd/^{144}Nd\right)_{measured}}{\left(^{143}Nd/^{144}Nd\right)_{CHUR}} - 1\right] \times 10000 \quad (1)$$

The fraction containing Sr after TRU-spec® resin separation was purified before Sr isotope analysis. Strontium was separated from the rest of the matrix on Sr-Spec® resin, using 3 mol.L^{-1} HNO_3 media, eluted with MiliQ water, evaporated, and dissolved in 0.05 mol. L^{-1} HNO_3 before isotopic measurement. The minimum amount of Sr required for isotopic measurement was 50 ng. The instrumental mass bias was corrected by normalizing to $^{86}Sr/^{88}Sr$ value of 0.1194. The SRM 987 was measured every five samples and corrected with the bracketing method. The certified value of 0.71034 is used for $^{87}Sr/^{86}Sr$ correction factor calculation. More details on Sr isotope ratio measurement can be found in Dessert et al. (2020). Three geostandards (MAG-1, QLO-1, and BHVO-1) were measured in addition to samples; the values reported in Table 2 agree well with signatures reported in the literature.

Atmospheric aerosols were sampled simultaneously, in the vicinity of the deposition collector, from 27 March 2017 to 28 May 2018, in steps of 1–2 weeks. The results were published in a recent study comparing the chemical composition and lead isotope ratios of aerosols and deposition samples (Xu-Yang et al., 2025). Aerosol samples containing at least 50 ng of neodymium total quantity in solution were analyzed for strontium and neodymium isotope ratios in the same way as the deposition samples.

2.5. Sea-Salt $^{87}Sr/^{86}Sr$ Ratio Correction

The equations used for sea salt $^{87}Sr/^{86}Sr$ ratio correction are the same for deposition samples and aerosol samples. The strontium isotope ratio measured in the deposition samples results from a mixture of both dust and sea-salt. The contribution of strontium from dust is calculated by subtracting the sea-salt strontium contribution from the total strontium. The strontium isotopic ratio of dust is calculated using mixing equations (e.g., Capo et al., 1998; Stewart et al., 1998; Whipkey et al., 2000) and a constant strontium isotopic ratio of sea salt: 0.70917 (Dia et al., 1992). The sea-salt contribution to total strontium is calculated using sea salt sodium and sea-salt composition (Brewer, 1975). Sea salt sodium is calculated by subtracting the crustal sodium from the measured total sodium (Rahn, 1976). The Rudnick and Gao (2014) crustal model is applied, using aluminum as a reference element to calculate the crustal sodium.

The $\left(^{87}Sr/^{86}Sr\right)_{total}$ is assumed to be explained by a two-end-member mixture of sea salt $\left(\left(^{87}Sr/^{86}Sr\right)_{sea\ salt}\right)$ and dust $\left(\left(^{87}Sr/^{86}Sr\right)_{dust}\right)$ as shown in Equation 2:

$$\left(^{87}Sr/^{86}Sr\right)_{total} = \%Sr_{sea\ salt} \times \left(^{87}Sr/^{86}Sr\right)_{sea\ salt} + \%Sr_{dust} \times \left(^{87}Sr/^{86}Sr\right)_{dust} \quad (2)$$

Table 2
Comparison of εNd *and* $\left(^{87}Sr/^{86}Sr\right)$ *Isotope Ratios Measured in MAG-1, QLO-1, and Two BHVO-1 Geostandards in the Present Study With Published Values*

	Measured $^{87}Sr/^{86}Sr$	Published $^{87}Sr/^{86}Sr$	Measured εNd	Published εNd
$BHVO-1$[a] (1)	0.70359 ± 0.00002	0.703475 ± 0.00002	6.5 ± 0.1	6.8 ± 0.2
$BHVO-1$[a] (2)	0.70358 ± 0.00002	0.703475 ± 0.00002	6.3 ± 0.15	6.8 ± 0.2
$MAG-1$[b]	0.72283 ± 0.00001	0.72274 ± 0.00001	−11.0 ± 0.1	−11.6 ± 0.2
$QLO-1$[c]	0.70400 ± 0.00001	0.70389 ± 0.00001	4.1 ± 0.15	4.1 ± 0.1

[a]Weis et al. (2005). [b]Nagender Nath et al. (2009). [c]Bao et al. (2018).

Then

$$\left(^{87}\mathrm{Sr}/^{86}\mathrm{Sr}\right)_{\mathrm{dust}} = \frac{\left(^{87}\mathrm{Sr}/^{86}\mathrm{Sr}\right)_{\mathrm{total}} - \%Sr_{\mathrm{sea\ salt}} \times \left(^{87}\mathrm{Sr}/^{86}\mathrm{Sr}\right)_{\mathrm{sea\ salt}}}{\%Sr_{\mathrm{dust}}} \tag{3}$$

where $\left(^{87}\mathrm{Sr}/^{86}\mathrm{Sr}\right)_{\mathrm{dust}}$ is the $^{87}\mathrm{Sr}/^{86}\mathrm{Sr}$ of dust to be calculated; $\left(^{87}\mathrm{Sr}/^{86}\mathrm{Sr}\right)_{\mathrm{sea\ salt}}$ is the $^{87}\mathrm{Sr}/^{86}\mathrm{Sr}$ of sea salt, presumed to be constant, with a value of 0.70917, as proposed by Dia et al. (1992); $\left(^{87}\mathrm{Sr}/^{86}\mathrm{Sr}\right)_{\mathrm{total}}$ is the value of $^{87}\mathrm{Sr}/^{86}\mathrm{Sr}$ measured in deposition samples, taken to be a mixture of sea salt and dust; $\%Sr_{\mathrm{sea\ salt}}$ and $\%Sr_{\mathrm{dust}}$ are the contribution of sea salt and dust to the total quantity of Sr, calculated using the following two equations.

The contribution of sea salt to the total quantity of Sr ($\%Sr_{\mathrm{sea\ salt}}$) is calculated using Equation 4:

$$\%Sr_{\mathrm{sea\ salt}} = \frac{Q(\mathrm{Sr})_{\mathrm{sea\ salt}}}{Q(\mathrm{Sr})_{\mathrm{total}}} = \frac{Q(Na)_{\mathrm{sea\ salt}} \times \left(\frac{\mathrm{Sr}}{Na}\right)_{\mathrm{sea\ salt\ model}}}{Q(\mathrm{Sr})_{\mathrm{total}}} \tag{4}$$

where $Q(\mathrm{Sr})_{\mathrm{total}}$ is the total quantity of Sr measured in a sample, taken to originate from sea salt and dust, $Q(\mathrm{Sr})_{\mathrm{sea\ salt}}$ is the quantity of Sr originating from sea salt. $\left(\frac{\mathrm{Sr}}{\mathrm{Na}}\right)_{\mathrm{sea\ salt\ model}}$ is equal to the Sr/Na ratio in sea salt: 0.000741 (Brewer, 1975). $Q(Na)_{\mathrm{sea\ salt}}$ is the quantity of sodium originating from sea salt, calculated using the following Equation 5:

$$Q(Na)_{\mathrm{sea\ salt}} = Q(Na)_{\mathrm{total}} - Q(Al)_{\mathrm{total}} \times \left(\frac{Na}{Al}\right)_{\mathrm{crust\ model}} \tag{5}$$

where $\left(\frac{Na}{Al}\right)_{\mathrm{crust\ model}}$ is equal to the Na/Al ratio in the upper continental crust: 0.298 (Rudnick & Gao, 2014); $Q(Na)_{\mathrm{total}}$ and $Q(Al)_{\mathrm{total}}$ are the total quantity of sodium and aluminum measured, as detailed in Xu-Yang et al. (2022).

The contribution of dust to the total Sr ($\%Sr_{\mathrm{dust}}$) is calculated using Equation 6:

$$\%Sr_{\mathrm{dust}} = 100\% - \%Sr_{\mathrm{sea\ salt}} \tag{6}$$

2.6. Compositional Data Analysis

A compositional covariance biplot is used for compositional data analysis, which consists of Principal Component Analysis (PCA) applied to centered log-ratio (clr) transformed data. The clr transformation is commonly performed to open the data before applying any multivariate techniques based on correlation:

$$clr(x) = \left[\ln\frac{x_1}{gm(\mathbf{x})}, \ldots, \ln\frac{x_D}{gm(\mathbf{x})}\right] \tag{7}$$

where $gm(\mathbf{x})$ denotes the geometric mean of the D parts: $gm(\mathbf{x}) = \left(\prod_{i=1}^{D} x_i\right)^{\frac{1}{D}}$. A PCA can then be computed on transformed data to summarize the structure of the data in a lower-dimensional space (usually two). On a compositional biplot, the length of a link between arrow heads of two rays represents the standard deviation of the log-ratio between these compositional parts (Suárez et al., 2016). The distance between individuals on a biplot reflects the compositional difference between samples. Individuals that are in the same region have a similar composition. The compositional biplot was produced using the "compositions" package of R software (R Core Team, 2018), which was specifically designed to analyze compositional data (van den Boogaart & Tolosana-Delgado, 2013). More details on compositional data analysis applied to atmospheric aerosol measurements are presented in Xu-Yang et al. (2021).

2.7. Backward Trajectory Analysis

Because of long-range transport and uncertainties associated with the transport altitude of Saharan dust, it is unrealistic to use backward trajectory analysis in an attempt to link crustal elements in a specific deposition or aerosol sample collected in the Caribbean region to specific source regions in Africa (Prospero et al., 2014). For elements derived from marine emissions or atmospheric pollution from surrounding countries, which are carried over shorter distances than crustal elements, backward trajectories can be used to identify the region of origin (Carslaw & Ropkins, 2012; Cutter, 1993). For more information about the origins of Se and Sb, backward trajectories were calculated with the Hybrid Single-Particle Lagrangian Integrated Trajectory (Hysplit) version 5.2 (Stein et al., 2015) based on the Global Data Assimilation System (GDAS). A backward trajectory ensemble ending at 15°58′50.84″N, 61°42′12.99″W at an altitude of 1,000 m above sea level was calculated. The backward trajectory length was 12 days in 1-hr steps, and an ensemble calculation was started for every hour during the entire sample collection period from 2015-03-01 to 2018-08-31. The choice of a 12-day backward trajectory is based on the previously estimated typical dust travel time from North Africa to the Americas (Ridley et al., 2012). There is much over-plotting when trajectories are represented as lines or points over the course of a year. As a result, it is helpful to grid the trajectory data and compute different statistics by taking latitude-longitude intervals into account. The trajectory frequencies for each grid cell were calculated and plotted using the "openair" R package with the "trajLevel" function (Carslaw & Ropkins, 2012; R Core Team, 2018) by levels of deposition flux of Sb, Se, Al (proxy for trans-Atlantic Saharan dust), and sea-salt Na (proxy for sea salt).

3. Results and Discussion

3.1. Isotopic Ratios: Strontium, Neodymium, and Lead

For atmospheric deposition samples, Figure 2 presents the temporal evolution of the dust deposition flux (from Xu-Yang et al., 2022), the isotopic signatures for εNd and $^{206}Pb/^{207}Pb$, and the enrichment factor of Pb relative to UCC (Rudnick & Gao, 2014). The εNd median value for all the samples analyzed (i.e., Nd content over 50 ng, collected before 2018) was -12.9 ± 0.3 (median absolute deviation, as defined in Heimburger, Losno, and Triquet (2013)). The annual median values for εNd were -13.0 ± 0.3 in 2015, -12.5 ± 0.5 in 2016, and -12.9 ± 0.2 in 2017. These values are very close to the annual average values: -13.0 ± 0.4 (standard deviation) for 2015, -12.5 ± 0.7 for 2016, and -12.7 ± 0.7 for 2017. The εNd values range from -13.5 to -10.6 for all the samples analyzed; these results are consistent with the typical range of values for dust derived from North Africa (-17.9 to -10.1) (Grousset & Biscaye, 2005; Grousset et al., 1998; Guinoiseau et al., 2022; Scheuvens et al., 2013; Skonieczny et al., 2011, 2013), and with previous studies on trans-Atlantic north-African dust measured during different periods and at different locations in the Caribbean region (Grousset et al., 1998; Kumar et al., 2014, 2018; Munroe et al., 2019; Pourmand et al., 2014; Zhao et al., 2018).

The $^{206}Pb/^{207}Pb$ ratio ranges from 1.159 to 1.213, with a median value of 1.184. The $^{208}Pb/^{207}Pb$ ratio ranges from 2.422 to 2.488, with a median value of 2.466. Strong seasonality is observed in the dust deposition flux, the lead isotope ratios, and the lead enrichment factor relative to UCC (Rudnick & Gao, 2014) (Figure 2).

The $\left(^{87}Sr/^{86}Sr\right)_{total}$ values, measured in the same set of samples as the εNd values, range from 0.71032 to 0.71442, with a median value of 0.7125 ± 0.0006 (median absolute deviation). These values are a mixture of both the sea-salt strontium isotope ratio (0.70917; Dia et al. [1992]) and the Saharan dust strontium isotope ratio (0.712–0.725 [Guinoiseau et al., 2022], for trans-Atlantic Saharan dust). After calculation using Equation 3, the $\left(^{87}Sr/^{86}Sr\right)_{dust}$ ranges from 0.7109 to 0.7168, with a median value of 0.7144 ± 0.0006 (median absolute deviation), highlighting the importance of correcting for the sea-salt contribution to assess the Saharan dust isotope ratio in the Caribbean region. For all the aerosol samples analyzed (i.e., Nd content over 50 ng), collected from 27 March 2017 to 28 May 2018 by Xu-Yang et al. (2025), $\left(^{87}Sr/^{86}Sr\right)_{total}$ ranges from 0.71110 to 0.71409, with a median value of 0.7127 ± 0.0005 (median absolute deviation); $\left(^{87}Sr/^{86}Sr\right)_{dust}$ ranges from 0.71333 to 0.71529, with a median value of 0.7143 ± 0.0005; εNd ranges from -13.9 to -12.1, with median value of -13.0 ± 0.5.

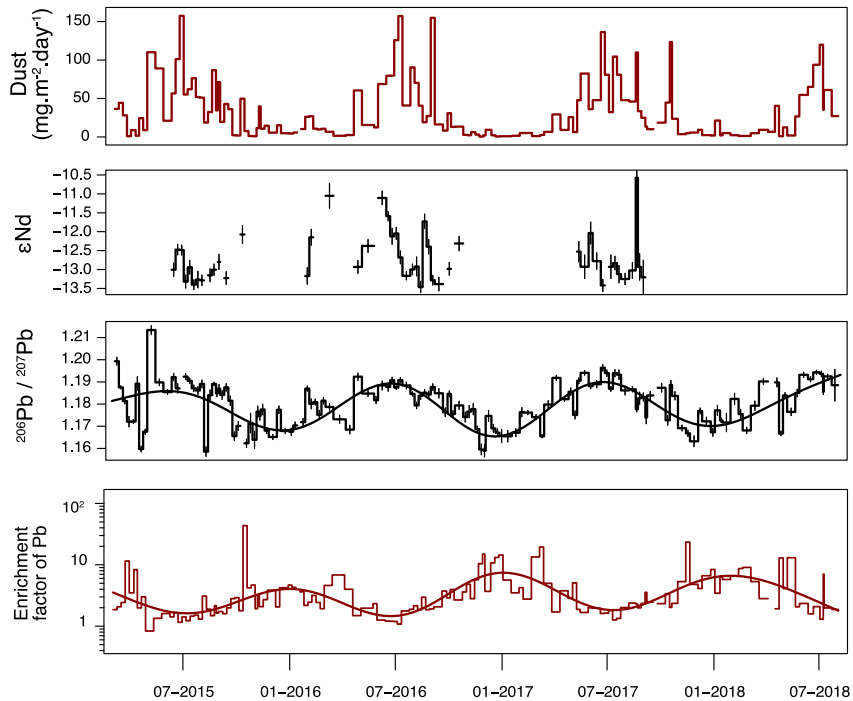

Figure 2. Temporal evolution of dust deposition flux $\left(\mathrm{mg.m^{-2}.day^{-1}}\right)$; εNd and $^{206}\mathrm{Pb}/^{207}\mathrm{Pb}$ ratios, and Pb enrichment factor relative to crustal Al from UCC (Rudnick & Gao, 2014) for deposition samples. For $\left(^{87}\mathrm{Sr}/^{86}\mathrm{Sr}\right)_{\mathrm{dust}}$ results, see Figure 3.

3.2. Potential Source Areas (PSAs)

Six potential source areas (PSAs) in North Africa were identified by Guinoiseau et al. (2022), who combined the available literature on the geochemical fingerprint of the fine fraction of surface soils with geological information for this region (Figure 1).

On the εNd versus $\left(^{87}\mathrm{Sr}/^{86}\mathrm{Sr}\right)_{\mathrm{dust}}$ diagram (Figure 3), almost all of the deposition and aerosol samples lie within PSA (LAM). The three outliers (all collected between June and September 2017) cannot be classified due to their slightly unusual isotopic signatures. Two other PSAs overlap PSA (LAM): PSA (BD) and PSA (WAC). The PSA (WAC) has a very similar εNd and elemental composition to PSA (LAM) (Guinoiseau et al., 2022), but should not be considered as a major source of dust transported to the Caribbean region due to its low dust source activation frequency over the whole year (Jewell et al., 2021), also visible in North African Sandstorm Survey (NASCube) images (Gonzalez & Briottet, 2017). In Guinoiseau et al. (2022), $\left(^{207}\mathrm{Pb}/^{204}\mathrm{Pb}\right)$ and $\left(^{208}\mathrm{Pb}/^{204}\mathrm{Pb}\right)$ data were used to eliminate PSA (BD) as a source for dust transported to locations on both sides of the Atlantic Ocean. This finding is consistent with satellite observation and trajectory analysis studies by Y. Yu et al. (2020), highlighting the limited potential for long-range transport of dust from the Bodélé Depression, attributed to extensive near-source dust removal by deposition during the boreal winter (dry) and summer (wet). Under specific climatic circumstances, however, PSA (BD) has been shown to deliver dust to the Amazon region. Barkley et al. (2022) detected species of freshwater diatoms from African paleolakes, suggesting a Bodélé origin, in the winter and spring of 2016 at Cayenne, together with inter-annual variation on the εNd and $\left(^{87}\mathrm{Sr}/^{86}\mathrm{Sr}\right)_{\mathrm{dust}}$ of trans-Atlantic dust in 2014 and 2016. The strength of the Libyan High could be one of the factors modulating the relative amount of dust transported from each PSA across the Atlantic Ocean (Barkley et al., 2022; Washington & Todd, 2005).

We therefore conclude that PSA (LAM) is the major source of dust transported across the Atlantic Ocean, whereas PSA (BD) may be a source under certain specific climatic circumstances. More research is necessary to evaluate the strength of PSA (BD) as a source of dust transported across the Atlantic Ocean, using the isotope ratios of $\left(^{207}\mathrm{Pb}/^{204}\mathrm{Pb}\right)$ and $\left(^{208}\mathrm{Pb}/^{204}\mathrm{Pb}\right)$, and removing the more labile anthropogenic Pb with mild acid (e.g., 0.5 M HBr). Continuous sampling of atmospheric deposition or aerosol samples will provide a window of

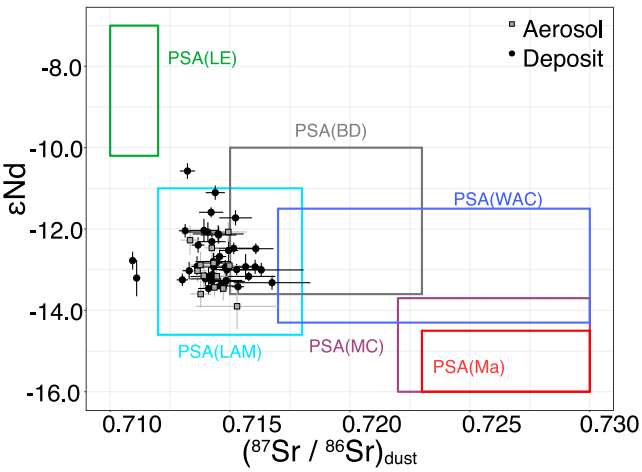

Figure 3. Identifying the most probable source areas through radiogenic isotope proxies [εNd versus $\left({}^{87}Sr/{}^{86}Sr\right)_{dust}$]. The colored rectangles delimit PSAs based on the standard deviations of all the εNd and ${}^{87}Sr/{}^{86}Sr$ values, taken from Figure 5(B) in Guinoiseau et al. (2022), where boxes for PSA (MC), PSA (Ma), and PSA (LE) extend beyond the values shown in the figure presented here. Solid black circles are deposition samples collected by Xu-Yang et al. (2022); and solid gray squares are aerosol samples collected by Xu-Yang et al. (2025). Five deposition samples and one aerosol sample were excluded due to the high sea-salt contribution to the total Sr ($\%Sr_{sea\ salt} > 60\%$).

opportunity for studies linking climate change and Saharan dust emission, transport, and fertilization in the Caribbean region.

3.3. Rare Earth Element (REE) Compositional Variation

Figure 4 plots the result of the REE compositional analysis (compositional biplot) for deposition samples collected during the entire sampling period. The REE profiles normalized to UCC (Rudnick & Gao, 2014) were also calculated and plotted in Figure A1. The first two principal components explain 76% of the variance. Compared with samples collected in 2016, the REE compositions of samples collected in 2015, 2017, and 2018 are quite stable, with no noticeable variation. The difference between the samples collected in 2016 and those collected in 2015, 2017, and 2018 is less obvious on the traditional REE profile plot (Figure A1), demonstrating the validity of the biplot as an efficient alternative method to study REE composition. The majority of the 2016 material is similar to the samples collected in 2015, 2017, and 2018 with similar stable REE patterns. Several of the 2016 samples fall outside the range of variability for REE composition (Comp.1). At this stage, it would be difficult to propose hypotheses for this apparent variability. The isotopic signatures [εNd and $\left({}^{87}Sr/{}^{86}Sr\right)_{dust}$] of the five most visibly different REE compositions in Figure 4 are within the normal range of values for PSA (LAM) (Table 3).

3.4. Origin and Enrichment Factors of Trace Elements in Atmospheric Deposition Samples

The temporal evolution of the total deposition flux and enrichment factors relative to crustal Al (Rudnick & Gao, 2014) and sea-salt Na (Brewer, 1975) for each element are plotted individually in Figures A2–A5. These figures show that Be, Sc, Ti, V, Cr, Mn, Co, and Ni are characteristic crustal elements in this dataset, exhibiting minimal fluctuation in the enrichment factor relative to crustal Al, always approximating 1. The enrichment factor relative to sea-salt Na is almost always higher than 100 for the same elements throughout the sampling period, implying that sea salt is a negligible source for these elements. Sea salt is a relatively important source for Sr and Mo; a clear seasonal transition between dust and sea salt as primary sources for these elements can be seen in Figure A4. Sea salt may also be a source for Rb and U, particularly from November to January when their deposition fluxes are the lowest; Saharan dust appears to be the predominant source from June to August and remains the most important source over the year. For V and Ni, significant non-sea-salt and non-crustal contributions in the winter months in 2017 and 2018 are observed, as shown by enrichment factors reaching 10 or more.

Enrichment factors relative to crustal Al (Rudnick & Gao, 2014) for the non-sea-salt fraction of trace elements in the atmospheric deposition samples are shown in Figure 5 (the subtraction of the sea-salt fraction is detailed in Xu-Yang et al. [2022]). The median values of enrichment factors for the non-sea-salt fraction of Pb (2.4), As (2.7), Mo (3.4), Cu (4.3), Sb (21.6), and Se (110.2) are higher than those of the other elements, suggesting that sources other than dust and sea salt may be particularly important for these elements. The contributions of sea salt and Saharan dust to the deposition fluxes of Pb, As, Mo, Cu, Sb, and Se (calculation presented in Xu-Yang et al. [2022]), as well as the excess fraction (defined as non-sea-salt and non-dust fraction [Xu-Yang et al., 2022]) of the deposition flux of these elements is presented in Table 4. The excess fraction is highest for Sb (96%) and Se (99%). The excess fraction is relatively high for Cu (78%), Mo (62%), As (56%), and Pb (50%), compared to the crustal and sea-salt fractions.

Automotive brake abrasion dust may contain antimony because antimony sulfide is used as a lubricant in brake pads. This traffic-related dust could be the predominant source of fine airborne particulate matter enriched in antimony (Jiang et al., 2021; Smichowski, 2008). Coal combustion emits antimony, predominantly as ultra-fine or fine particle fractions (e.g., Pavageau et al., 2002); it may therefore be an important source of atmospheric antimony (Jiang et al., 2021). Antimony is used to produce polyester and flame retardants for plastics and textiles; incineration of these materials releases aerosols rich in antimony (Paoletti et al., 2001). Enrichment factors for

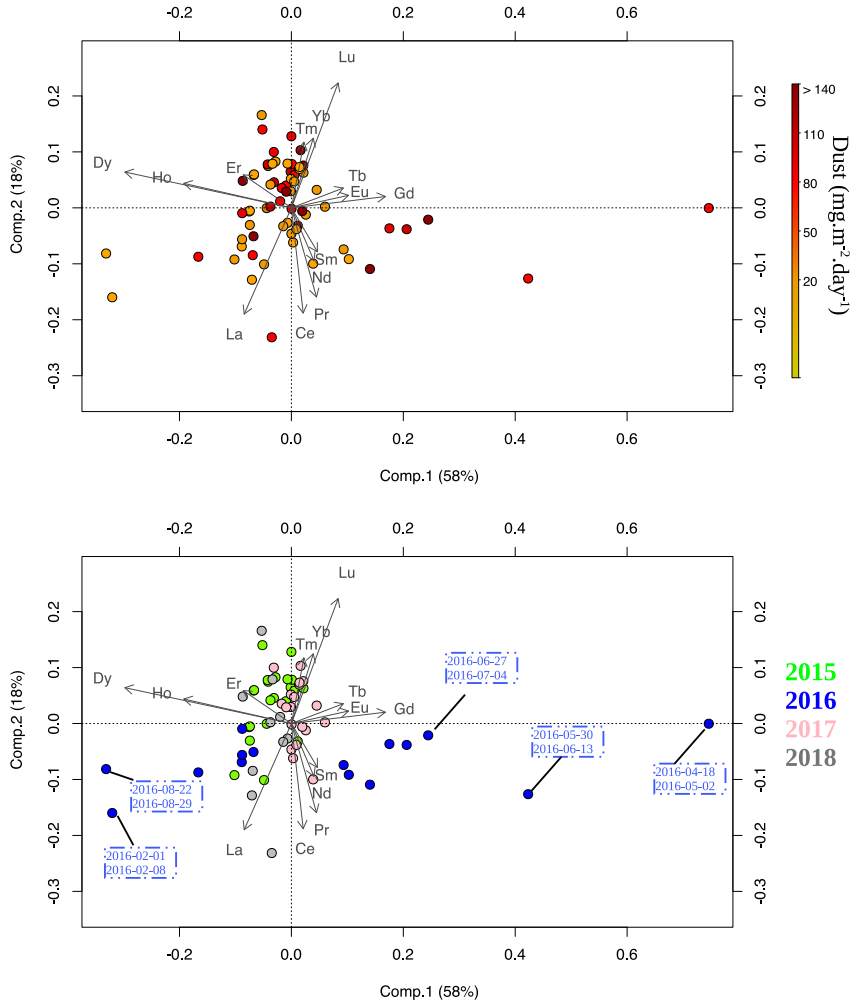

Figure 4. Compositional biplot for samples with a deposition flux over 20 mg.m^{-2}.day^{-1} (65 samples in total). (a) Samples collected during different years are plotted on the same figure. The color gradient indicates the strength of the dust deposition flux. (b) Different colors indicate different years. The dust deposition flux has no impact on REE composition. The REE composition for samples collected in 2016 is more variable than those of samples collected in 2015, 2017, and 2018. Sampling periods are shown for the five most visibly different REE compositions, all from 2016.

antimony in our samples are consistent with the review study by Jiang et al. (2021), which found 100–1,000 for most of the suspended airborne particles (total, PM2.5 and PM10) collected around the world. During the sampling period, a progressive increase in the antimony deposition flux is observed, as shown in Figure A4.

Around 65% of global atmospheric selenium is biogenic; it is emitted from the marine and terrestrial biosphere as organic selenium. The remaining 35% is of anthropogenic origin, emitted as inorganic selenium (Feinberg,

Table 3
Data for the Five Samples Presenting Visibly Different REE Compositions in Figure 4

Date 1	Date 2	Dust deposition flux (mg·m^{-2}·day^{-1})	εNd	$(^{87}Sr/^{86}Sr)_{dust}$	Supposed origin
2016-04-18	2016-05-02	60	−12.931	0.7160	PSA (LAM)
2016-05-30	2016-06-13	69	−11.106	0.7144	PSA (LAM)
2016-06-27	2016-07-04	126	−12.044	0.7131	PSA (LAM)
2016-02-01	2016-02-08	27	−12.147	0.7145	PSA (LAM)
2016-08-22	2016-08-29	27	−12.394	0.7137	PSA (LAM)

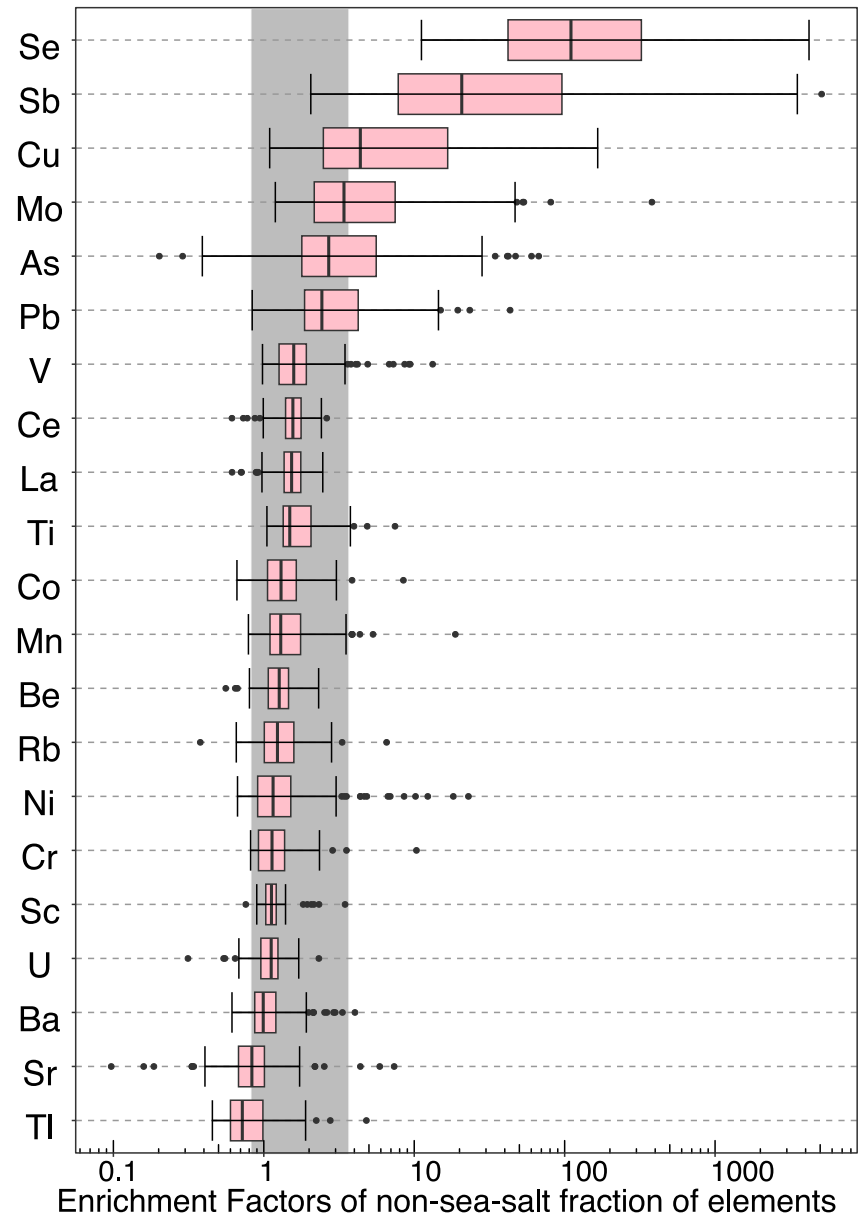

Figure 5. Enrichment factors of the non-sea-salt fraction of trace elements relative to UCC, from Rudnick and Gao (2014). Gray area shows the range from 0.8 to 4, the range of values currently observed for elements sourced from natural dust, according to Lawrence and Neff (2009). The non-sea-salt fraction for each element is calculated by subtracting the sea-salt fraction from the total atmospheric deposition flux, as detailed in Xu-Yang et al. (2022).

Maliki, et al., 2020; Feinberg, Stenke, et al., 2020). The contribution from sea salt and dust is negligible for atmospheric selenium (Feinberg, Stenke, et al., 2020). Both selenium and arsenic can be emitted via bio-methylation and subsequent volatilization from the biosphere (Vriens et al., 2014). It has been suggested that the formation pathways for methylated selenium and arsenic compounds are analogous to that for dimethyl sulfide $(CH_3)_2S$, since the (bio)geochemistry of selenium and arsenic is closely interlinked with sulfur in many environments (Langner et al., 2012; Stefels et al., 2007). In a previous study, Breuninger, Tolu, Thurnherr, et al. (2024) showed that air parcels can accumulate organic selenium during transport in regions with active marine productivity. Cutter (1993) showed that inorganic anthropogenic selenium can be enriched in air parcels passing over North America. Positive correlation has been found for As, S, and Se in both biogenic and anthropogenic emissions (Breuninger, Tolu, Thurnherr, et al., 2024; Cutter, 1993; Feinberg, Stenke, et al., 2020). Such correlation is also observed in the present study, as shown in Figure A6.

Table 4
Mean Atmospheric Deposition Fluxes and Major Source Contributions of the Highly Enriched Elements in Guadeloupe

	Total[a] ($ng \cdot m^{-2} \cdot day^{-1}$)	Marine contribution	Crustal contribution (%)	Excess (%)
Se	210	Around 0.1%	1	99
Sb	360	0.1%	3	96.5
Cu[b]	3,800	Around 0.02%	22	78
Mo	120	11%	28	62
As[c]	345	1%	43	56
Pb	1,040	Around 0.01%	50	50

Note. The contributions of sea salt and Saharan dust to the deposition of these elements is calculated in the same way as for major elements detailed in Xu-Yang et al. (2022), using the sea-salt composition model (Brewer, 1975) and the crustal composition model (Rudnick & Gao, 2014). [a]Weighted mean total deposition flux (wet + dry). [b]One sample, collected between 27 April 2015, and 11 May 2015, exhibits an excessively high Cu concentration and is excluded from calculations involving copper. [c]The As values are under the detection limit in six samples, and these values are replaced with half of the detection limit.

The anthropogenic and biogenic origin of antimony and selenium, as explained in the paragraphs above, appears to be supported by Figures A7–A9. When compared to periods with the lowest deposition fluxes of excess-Se and of excess-Sb, the period with the highest deposition fluxes during our study corresponds to a period with air parcels spending more time in and traveling through a zone situated in the latitude band between 30° and 60°N in the Atlantic Ocean and North America (Figure A7 marked by a black oval in each figure). This zone encompasses the Sargasso Sea and a part of North America. Air mass from Europe can also be transported to this altitude band, suggesting that atmospheric pollution from North America and Europe may be a significant source of Sb and Se. Biogenic gas from the Sargasso Sea may also contribute to high levels of Se. A similar trend is observed for sea-salt sodium (Figure A10) but not for aluminum (Figure A11). Further studies on arsenic and selenium speciation and antimony isotopes in deposition or aerosol samples should lead to better source analysis of these elements in the Caribbean region, to calculate the anthropogenic versus natural contributions of these elements (Breuninger, Tolu, Aemisegger, et al., 2024; Breuninger, Tolu, Thurnherr, et al., 2024).

The deposition flux of the excess fraction is less significant for the remaining elements (Cu, Mo, and Pb). The excess fraction of molybdenum (62%) in the current study aligns with the review and model analysis of Wong et al. (2021), which indicates that 40%–75% of atmospheric molybdenum is derived from anthropogenic sources, predominantly from smelting, coal combustion, and brake dust. Copper is observed to be systematically enriched in atmospheric aerosols. Anthropogenic atmospheric copper emissions are estimated to be of similar magnitude to natural emissions (Pacyna & Pacyna, 2001). Copper of natural or anthropogenic origin can be enriched in the sea surface layer and be emitted in air by bubble bursting (Cattell & Scott, 1978; Marsay et al., 2022). The Bubble Interfacial Microlayer Sampler was used in the North Atlantic (Sargasso Sea) to determine the enrichment factors, relative to sea-salt sodium, for a series of trace metals, finding an enrichment factor of 800 for copper, 20,000 for zinc, and 4,000 for lead (Weisel et al., 1984). If we use these enrichment factors as a scaling factor to correct the marine contribution to these elements (see details in Marsay et al., 2022), then the marine contribution will be 16% (Cu), 40% (Pb), and 200% (Zn), which can partly explain the excess fraction 78% (Cu), 50% (Pb), and 97% (Zn) observed in the present study and Xu-Yang et al. (2025), although the scaling factors vary considerably in the literature (Marsay et al., 2022).

3.5. Lead From Unidentified Anthropogenic Sources

Lead isotope ratios, depicted as $^{206}Pb/^{207}Pb$ versus $^{208}Pb/^{207}Pb$ by level of lead enrichment factor relative to crustal aluminum (Figure 6) show mixing between at least two end members. A strong relationship is observed between lead isotope ratios and lead enrichment factors. The atmospheric deposition samples collected during dusty periods with low lead enrichment factors fall on the mixing line trending toward the natural Saharan end member, where PSA (WAC), PSA (BD), and PSA (LAM) overlap, suggesting a larger contribution of lead associated with Northern African dust during these periods. The PSA (LAM) is potentially the most important end member, as PSA (BD) is not a major source of trans-Atlantic dust, according to Guinoiseau et al. (2022) and Y. Yu et al. (2020), and PSA (WAC) is excluded by Figure 3. The center of the zone defined by PSA (LAM)

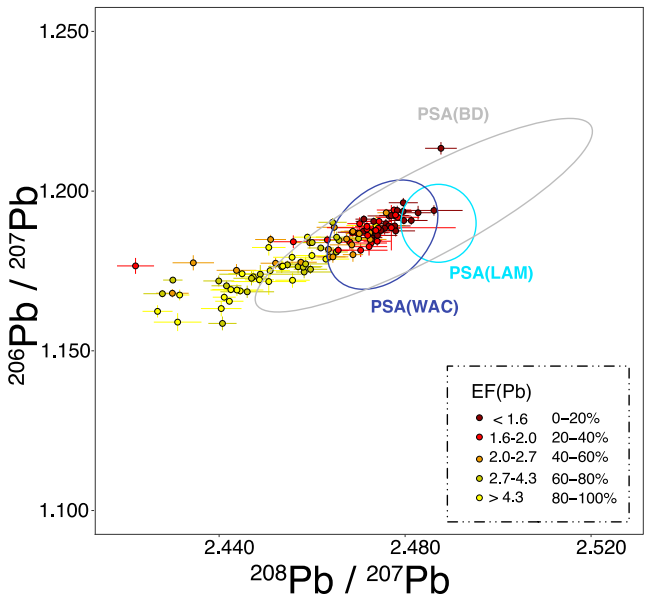

Figure 6. Lead isotope ratios ($^{206}Pb/^{207}Pb$ vs. $^{208}Pb/^{207}Pb$) by level of lead enrichment factor for deposition samples. The lead enrichment factors are represented by a color scale. Samples are separated into five levels, with 20% of the sample at each level: yellow for high enrichment factors (low dust deposition flux); red for low enrichment factors (high dust deposition flux). Error bars represent the 95% confidence interval. The PSA zones are defined from Guinoiseau et al. (2022) and Abouchami et al. (2013). PSA (LE), PSA (MC), and PSA (Ma) are not shown as they are excluded by the εNd versus $(^{87}Sr/^{86}Sr)_{dust}$ plot in Figure 3.

(Figure 6) is located at the end of the mixing line between natural and anthropogenic end members, confirming PSA (LAM) as the most probable source area. Samples collected during periods with low dust deposition flux present high enrichment factors and fall on the mixing line trending toward unidentified anthropogenic end members. For samples located near the lower-left end-member of the mixing line, and with enrichment factors over 4.3, the lead isotope signatures are around 1.16–1.17 for $^{206}Pb/^{207}Pb$ and 2.43–2.44 for $^{208}Pb/^{207}Pb$. For such samples, there is a mix of around 75%–80% of anthropogenic and 20%–25% of natural lead. With a two-end-member mixing equation, we obtain an anthropogenic signature of 1.14 for $^{206}Pb/^{207}Pb$ and 2.40 for $^{208}Pb/^{207}Pb$. Similar values for anthropogenic end-members are also defined by Witt et al. (2006) and Kumar et al. (2014) for aerosols collected in the Caribbean region. Over time, since the review studies of Bollhöfer and Rosman (2000, 2001), the isotopic signatures of anthropogenic end members must have changed due to changes in the source of lead added to gasoline and changes in the principal sources of lead in atmospheric pollution after the ban on leaded gasoline (Komárek et al., 2008; Monna et al., 2012). Furthermore, the problem with the $^{206}Pb/^{207}Pb$ versus $^{208}Pb/^{207}Pb$ plot is that the geological sources of Pb are very restricted in their position on this type of diagram. As shown in Figure A12, different anthropogenic end members all plot on the same linear array as samples from the present study. Many anthropogenic end members overlap, making it difficult to distinguish between them. It has been shown that most terrestrial lead is co-linear in this type of diagram (Ellam, 2010), implying that it is not best adapted to reveal multiple sources of lead. As a consequence, no reliable conclusions can be derived on the natural and geographic origin of this unknown anthropogenic end-member. For source-tracing studies using lead isotopes, measurement and new assessment of lead isotope signatures involving ^{204}Pb in aerosol samples collected worldwide between 2016 and 2018 would constrain the anthropogenic end-member for different regions and countries.

3.6. Comparing the Measured Deposition Fluxes of Trace Elements With Other Studies and Global Models

Recent publications (Xu-Yang et al., 2022, 2025) presented detailed comparisons for Saharan dust and sea salt deposition fluxes, scavenging ratios, and deposition velocity, based on our measurements, previous research in nearby regions, and model predictions.

This section therefore focuses only on elements that may have sources other than Saharan dust and sea salt.

Table 5 lists the measured total deposition flux of these elements (Se, Sb, Cu, Mo, As, and Pb) from this study, the measured total or wet deposition flux values from other studies in adjacent regions, and model predictions. Total deposition and wet deposition studies are comparable, as wet deposition forms the major part of total atmospheric deposition (Kadko et al., 2020; Mahowald et al., 2011; Xu-Yang et al., 2025). Furthermore, in many of the studies in Table 5, the wet deposition samples include dry deposition when collected by open funnel. Total deposition flux values measured in the current study are in good agreement with the model predictions for Se (Feinberg, Maliki, et al., 2020) and Mo (Wong et al., 2021) for the region. Measured values from adjacent regions show great variability. Deposition flux in Florida (wet, Landing et al., 2010) and Cuba (total, Morera-Gómez et al., 2019) are measured in polluted regions: near a coal-fired power plant (Florida site); downwind of a highly populated city with high traffic density and industrial activities (Cuban site). Hence, Se, As, and Pb deposition fluxes are higher for the Florida site (wet, Landing et al., 2010) than in Guadeloupe (total), while the Sb deposition flux is higher in Guadeloupe than in Florida (wet, Landing et al., 2010). The Sb, Cu, Mo, As, and Pb deposition fluxes are systematically higher at the Cuban site (total, Morera-Gómez et al., 2019) than in Guadeloupe (total). Deposition fluxes of Sb, Se, and As measured in Guadeloupe (total) are higher than those measured in 1986 in Bermuda (wet,

Table 5
Comparison Between Exposition Period Weighted Mean Atmospheric Deposition Fluxes Measured During the Present Study, Previous Studies in Adjacent Regions, and Model Prediction

	Total[a] ($ng \cdot m^{-2} \cdot day^{-1}$)	Nearby measurement ($ng \cdot m^{-2} \cdot day^{-1}$)	Model prediction ($ng \cdot m^{-2} \cdot day^{-1}$)
Se	210	90–120 (Bermuda and western Atlantic Ocean[b]); 1,130 (Florida[c])	30–300[d]
Sb	365	14 (Bermuda[b]); 210 (Florida[c]); 2,300 (Cuba[e])	–
Cu	3,800	8,800 (Cuba[e])	–
Mo	120	310 (Cuba[e])	55–110[f]
As	345	27 (Bermuda[b]); 850 (Florida[c]); 1,200 (Cuba[e])	–
Pb	1,040	1,350 (Florida[c]); 6,400 (Cuba[e])	–

[a]Weighted mean total deposition flux (wet + dry). [b]Cutter and Church (1986); Cutter (1993) wet deposition (measured around 1986 and 1993). [c]Landing et al. (2010) wet deposition (measured between 2005 and 2007). [d]Feinberg, Maliki, et al. (2020) model estimation. [e]Morera-Gómez et al. (2019) total deposition (measured between 2014 and 2016). [f]Wong et al. (2021) model estimation.

Cutter, 1993; Cutter & Church, 1986), an island situated in the subtropical west Atlantic Ocean, 1,800 km from Guadeloupe.

Rapid industrial and urban evolution worldwide contribute substantially to the spatial and temporal variability of the deposition fluxes of these elements.

4. Conclusions

The total atmospheric deposition flux of 33 trace elements is quantified in Guadeloupe in the Caribbean region between March 2015 and August 2018, by direct atmospheric deposition measurements. A multi-proxy approach is used to study the geographic origin of these elements and to differentiate anthropogenic sources from natural sources. The enrichment factors relative to UCC and sea salt suggest that, for our measurement site in Guadeloupe, Be, Sc, Ti, Rb, V, Cr, Mn, Co, and Ni are typical crustal elements originating from trans-Atlantic Saharan dust. The Sr and Nd isotopic signatures [$\left(^{87}Sr/^{86}Sr\right)_{dust}$ and εNd] indicate the Libya-Algeria-Mali region [PSA (LAM)] of the western Sahara as the principal source of dust delivered to the Caribbean. This result is consistent with previous geochemical and modeling studies conducted in the Caribbean region. Some minor inter-annual variation in REE composition was detected due to the 2016 samples, whereas the samples collected in 2015, 2017, and 2018 present stable profiles. These results suggest homogenized Saharan dust composition during transport. Because of the lack of REE compositional data over North African regions in general, and in the trans-Atlantic dust source region [PSA (LAM)] in particular, no explanation can be proposed to explain the inter-annual variation in REE compositions. The biplot graph of REEs is shown to be a powerful tool to explore REE compositional variations and study the source variations induced by climatic events and global climatic changes. For strontium and molybdenum, both sea salt and Saharan dust are major sources; for other trace elements (Sb, Cu, Se, and As), crustal and marine emissions are minor sources, whereas anthropogenic and biogenic emissions are major sources. Backward air mass trajectories link elevated antimony to pollution from North America and Europe and high selenium to biogenic emissions from the Sargasso Sea, both transported from the 20°–60°N Atlantic latitudinal band. The $^{206}Pb/^{207}Pb$ versus $^{208}Pb/^{207}Pb$ diagram shows that the lead results from the mixing between the Saharan dust end member and a potential anthropogenic end member still to be defined by new assessments of lead isotope emissions between 2015 and 2018 worldwide. The current dataset will provide a valuable resource to study total atmospheric deposition and its contribution to the terrestrial and marine biogeochemical cycles of the Caribbean region and the North Tropical Atlantic Ocean.

Appendix A: Validation of Analytical Methods

A1. Limits of Detection (LoD)

The limits of detection for total atmospheric deposition and for each element are calculated and listed in Table A1: 27 procedure blanks are prepared for ICP-MS, and 23 for ICP-AES with acid digestion; 17 field blanks are prepared for total atmospheric deposition samples.

Table A1
Field Limits of Detection (LoD) for Total Atmospheric Deposition Flux

Elements	Al	Ba	Ca	Fe	K	Li	Mg	Mn
Method	AES	AES	AES	AES	Flame	AES	AES	AES
LoD deposition $\mu g \cdot m^{-2} \cdot day^{-1}$	35	2	204	16	69	0.01	11	0.3
Elements	Na	P	S	Sc	Sr	Ti	Zn	Be
Method	Flame	AES	AES	AES	AES	AES	AES	MS (LR)
LoD deposition $\mu g \cdot m^{-2} \cdot day^{-1}$	54	48	14	0.05	0.12	9.03	1.15	0.002
Elements	Rb	Mo	Cd	Sb	Tl	Pb	U	V
Method	MS (LR)	MS (LR)	MS (LR)	MS (LR)	MS (LR)	MS (LR)	MS (LR)	MS (MR)
LoD deposition $\mu g \cdot m^{-2} \cdot day^{-1}$	0.039	0.05	0.005	0.074	0.0004	0.051	0.003	0.06
Elements	Cr	Co	Ni	Cu	As	Se	La	Ce
Method	MS (MR)	MS (MR)	MS (MR)	MS (MR)	MS (HR)	MS (HR)	MS (HR)	MS (HR)
LoD deposition $\mu g \cdot m^{-2} \cdot day^{-1}$	0.1	0.02	0.009	0.7	0.1	0.01	0.03	0.08
Elements	Pr	Nd	Sm	Eu	Gd	Tb	Dy	Ho
Method	MS (HR)	MS (HR)	MS (HR)	MS (HR)	MS (HR)	MS (HR)	MS (HR)	MS (HR)
LoD deposition $\mu g \cdot m^{-2} \cdot day^{-1}$	0.01	0.04	0.01	0.002	0.008	0.002	0.007	0.001
Elements	Er	Tm	Yb	Lu				
Method	MS (HR)	MS (HR)	MS (HR)	MS (HR)				
LoD deposition $\mu g \cdot m^{-2} \cdot day^{-1}$	0.003	0.001	0.003	0.0004				

Note. AES: ICP-AES. MS: ICP-MS. LR, MR, HR: measurements in low-, medium-, and high-resolution modes, respectively, using ICP-MS. The 17 field blanks were used to check the memory effect of the sampling system by rinsing the funnel a second time with 50 mL of a 3% v:v HCl water solution after sampling. The LoD is defined as three times the standard deviation of the quantity measured in field blanks. In order to facilitate comparison with the measured values, LoDs are expressed in terms of deposition flux by dividing by the surface of the funnel (0.0113 m^{-2}) and a 10-day exposure period.

A2. Validation of Analysis Method Using Geostandard Measurements

Nine finely ground geostandards (MAG-1, SCO-1, STM-1, SDC-1, BHVO-1, LKSD-2, BE-N, QLO-1, and BHVO-1 from USGS) were also prepared following the same digestion procedure as the deposition samples to validate the digestion procedures. Geostandards were hand-crushed for 30 min in an agate mortar to approximate aerosol grain size. To obtain a mass as close as possible to field atmospheric deposition samples, a few milligrams of the powders produced were digested. The results for recovery rate are listed in Table A2. Taking into account all the geostandards, the median value and average value of recovery rate for each element range from 80% to 120%, except for Tm (median value 79%) and Yb (median value 78%).

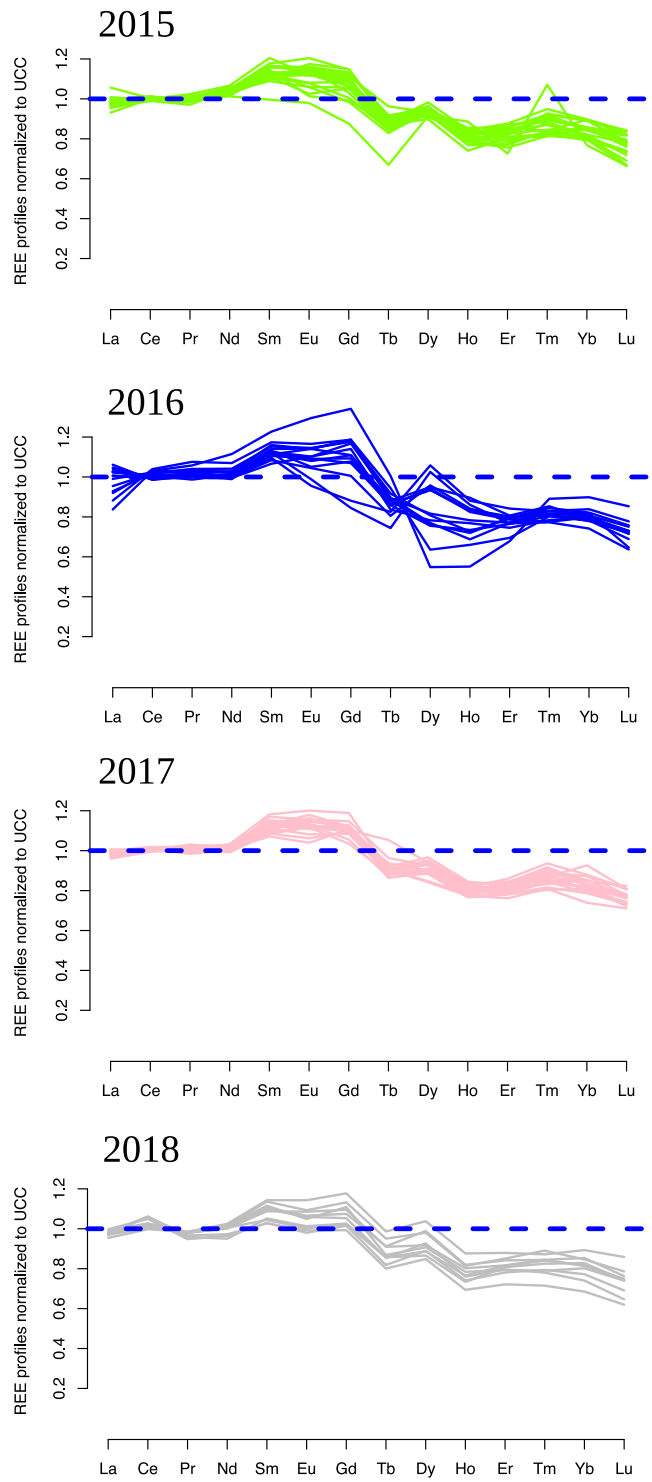

Figure A1. REE profiles of atmospheric deposition samples presenting dust deposition fluxes over 20 $mg.m^{-2}.day^{-1}$ (65 samples in total), normalized to UCC (Rudnick & Gao, 2014) for each year.

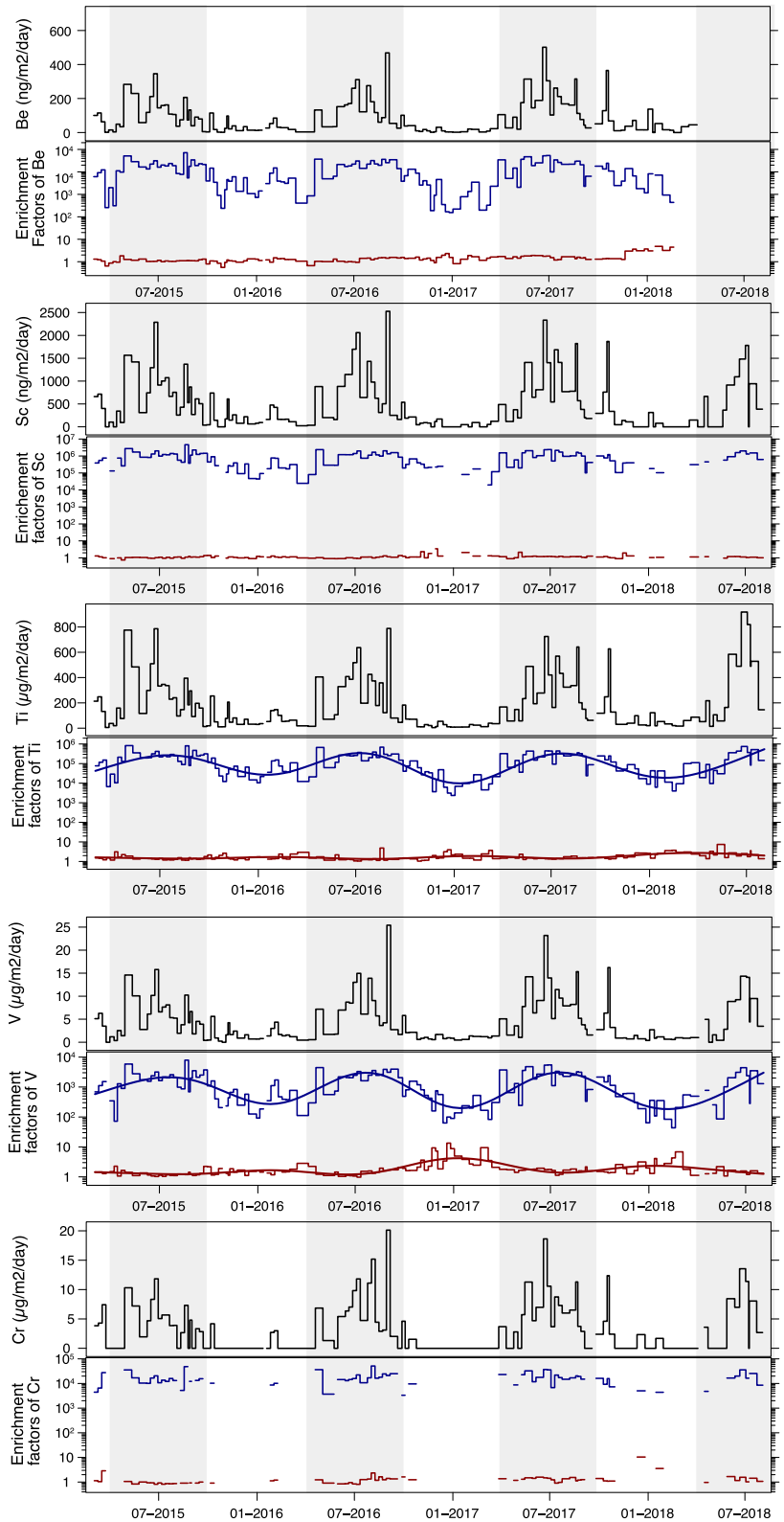

Figure A2. Deposition fluxes and enrichment factors of Be, Sc, Ti, V, and Cr. Enrichment factors relative to crust are in red and sea salt in blue. Gray zones mark the 1 April–30 September period for 2015, 2016, and 2017, and the 1 April–3 August period for 2018. For deposition fluxes, values below the quantification limit are set to 0 and are not plotted for enrichment factors. Enrichment factors for all elements are in log scale. All elements are only sourced from Saharan dust. The overlaid lines are smoothed curves generated using the timePlot function from the "openair" R package (Carslaw & Ropkins, 2012; R Core Team, 2021).

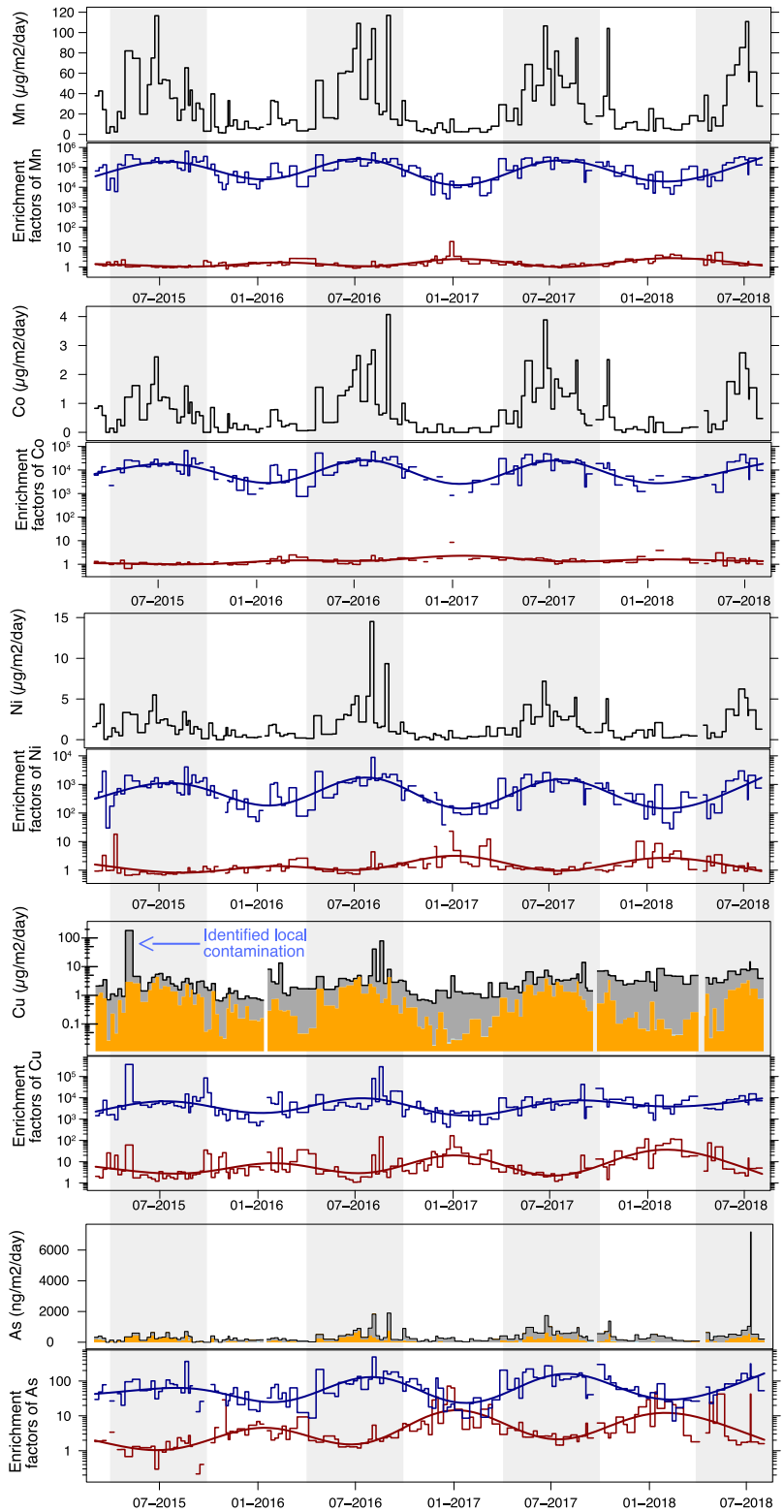

Figure A3. Deposition flux and enrichment factors of Mn, Co, Ni, Cu, and As. Enrichment factors relative to crust are in red and sea salt in blue. Gray zones mark the 1 April–30 September period for 2015, 2016, and 2017, and the 1 April–3 August period for 2018. For deposition fluxes, values below the quantification limit are set to 0 and are not plotted for enrichment factors. Enrichment factors for all elements and the deposition flux of Cu are in log scale. For Cu and As, the contribution of Saharan dust is shown in orange, that of sea salt in light-blue, with the non-attributed source in gray. Other elements are only sourced from Saharan dust. The overlaid lines are smoothed curves generated using the timePlot function from the "openair" R package (Carslaw & Ropkins, 2012; R Core Team, 2021).

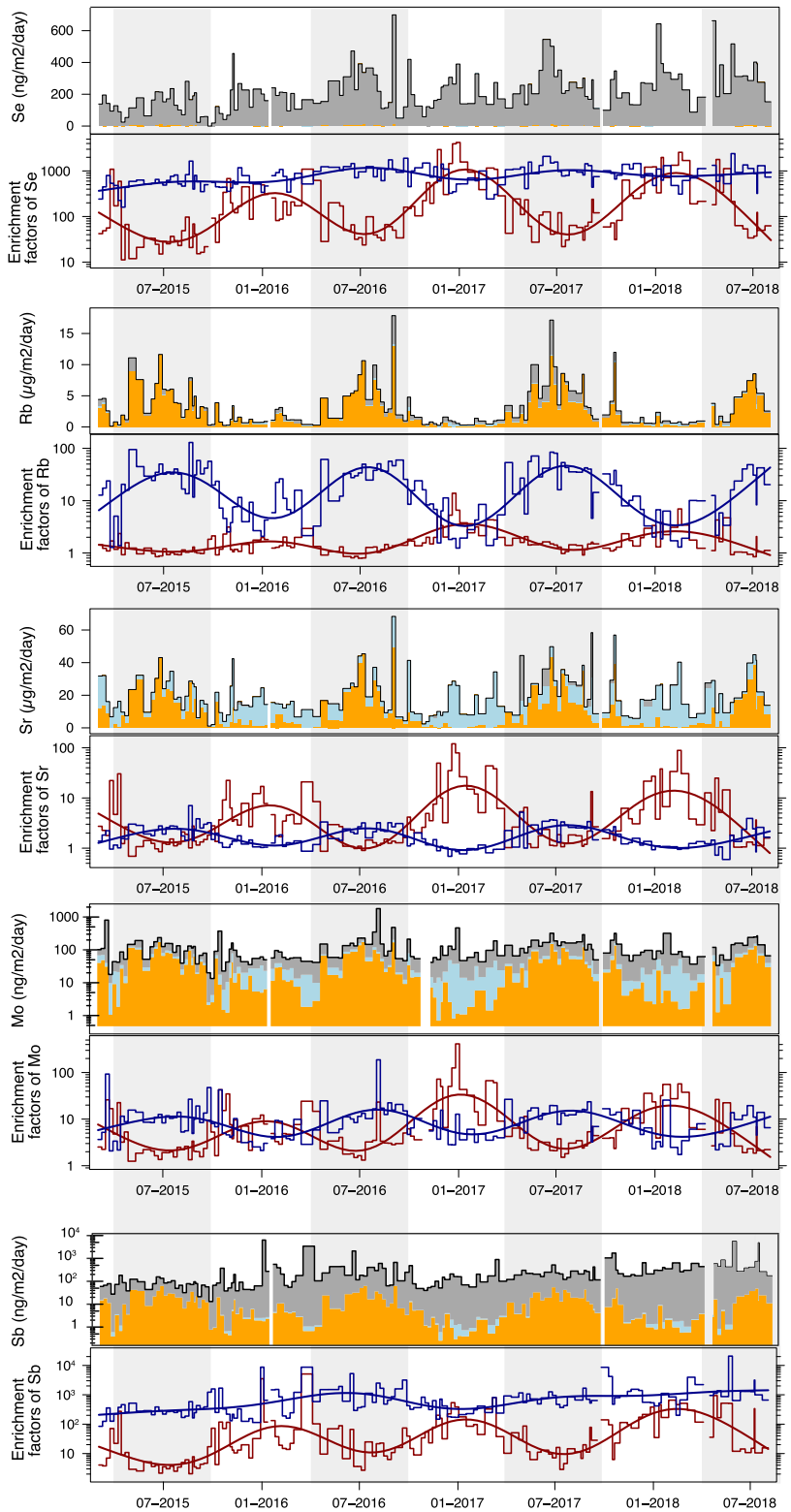

Figure A4. Deposition flux and enrichment factors of Se, Rb, Sr, Mo, and Sb. Enrichment factors relative to crust are in red and sea salt in blue. Gray zones mark the 1 April–30 September period for 2015, 2016, and 2017, and the 1 April–3 August period for 2018. For deposition fluxes, values below the quantification limit are set to 0 and are not plotted for enrichment factors. Enrichment factors for all elements and the deposition flux of Mo and Sb are in log scale. For each element, the contribution of Saharan dust is shown in orange, that of sea salt in light-blue, with the non-attributed source in gray. The overlaid lines are smoothed curves generated using the timePlot function from the "openair" R package (Carslaw & Ropkins, 2012; R Core Team, 2021).

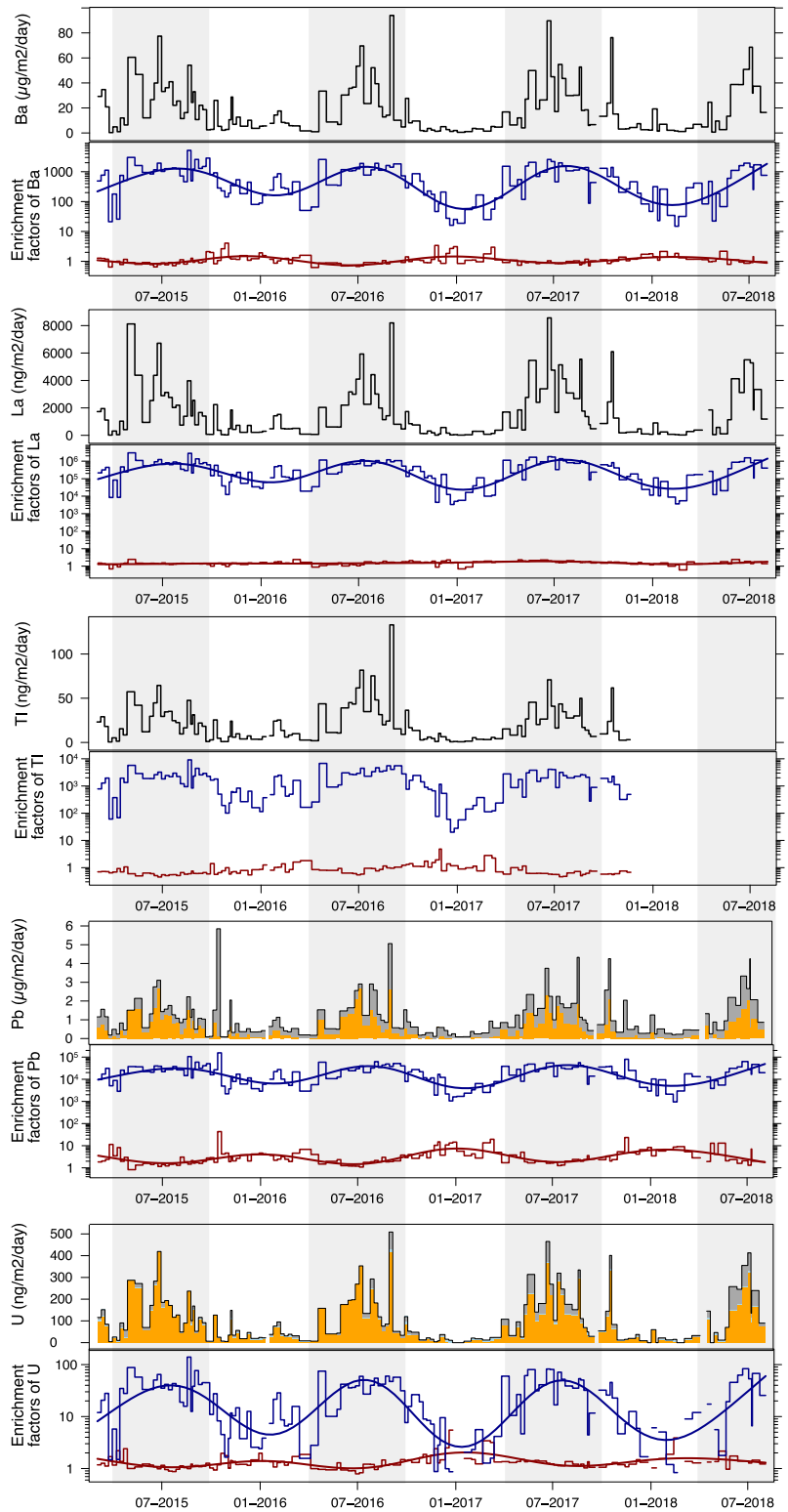

Figure A5. Deposition flux and enrichment factors of Ba, La, Tl, Pb, and U. Enrichment factors relative to crust are in red and sea salt in blue. Gray zones mark the 1 April–30 September period for 2015, 2016, and 2017, and the 1 April–3 August period for 2018. For deposition fluxes, values below the quantification limit are set to 0 and are not plotted for enrichment factors. Enrichment factors for all elements are in log scale. For Pb and U, the contribution of Saharan dust is shown in orange, that of sea salt in light-blue, with the non-attributed source in gray. Other elements are only sourced from Saharan dust. The rare earth elements are primarily sourced from Saharan dust and exhibit very similar trends; therefore, only lanthanum (La) is presented. The overlaid lines are smoothed curves generated using the timePlot function from the "openair" R package (Carslaw & Ropkins, 2012; R Core Team, 2021).

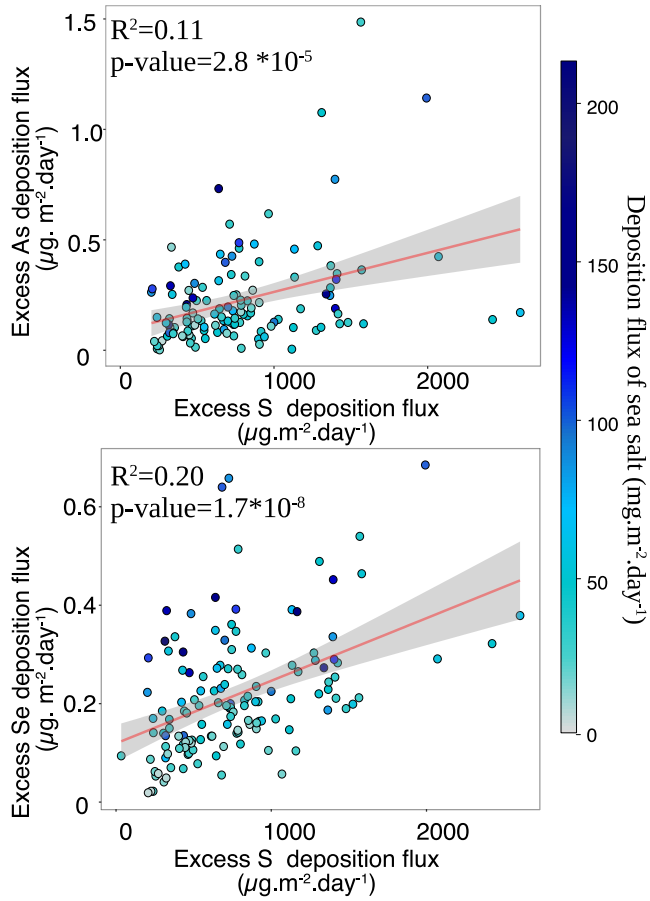

Figure A6. Excess deposition fluxes of As and Se as a function of excess deposition flux of S by level of sea salt deposition flux, showing a slight positive and statistically significant correlation between these three elements, despite the dispersion of the data points. The red line is a simple linear regression line with 95% confidence band presented by gray shaded area. The *p*-value of Pearson correlation is also given (<0.05 means that the correlation is statistically significant and >0.05 means that the correlation is not statistically significant).

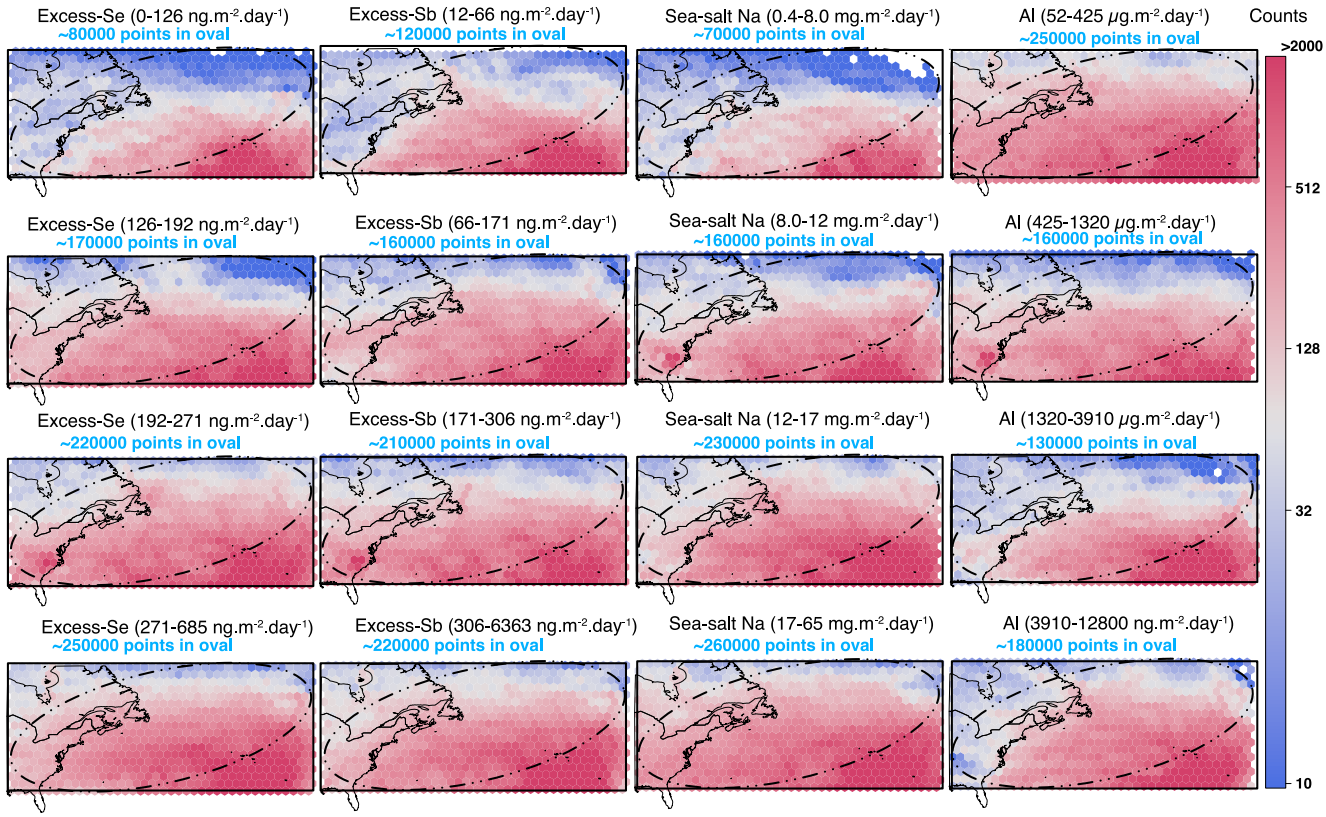

Figure A7. Gridded backward trajectory frequencies (arrival height: 1,000 m) with hexagonal binning by level of deposition fluxes of excess Se, excess Sb, sea-salt Na, and Al; each panel presents one quartile of data sorted by the deposition flux of one of these elements. Figures A8–A11 depict a wider geographic area. The ellipse marks a likely source region: air masses spending longer there are more enriched in Se, Sb, and sea salt due to longer exposure to marine aerosols and anthropogenic pollution.

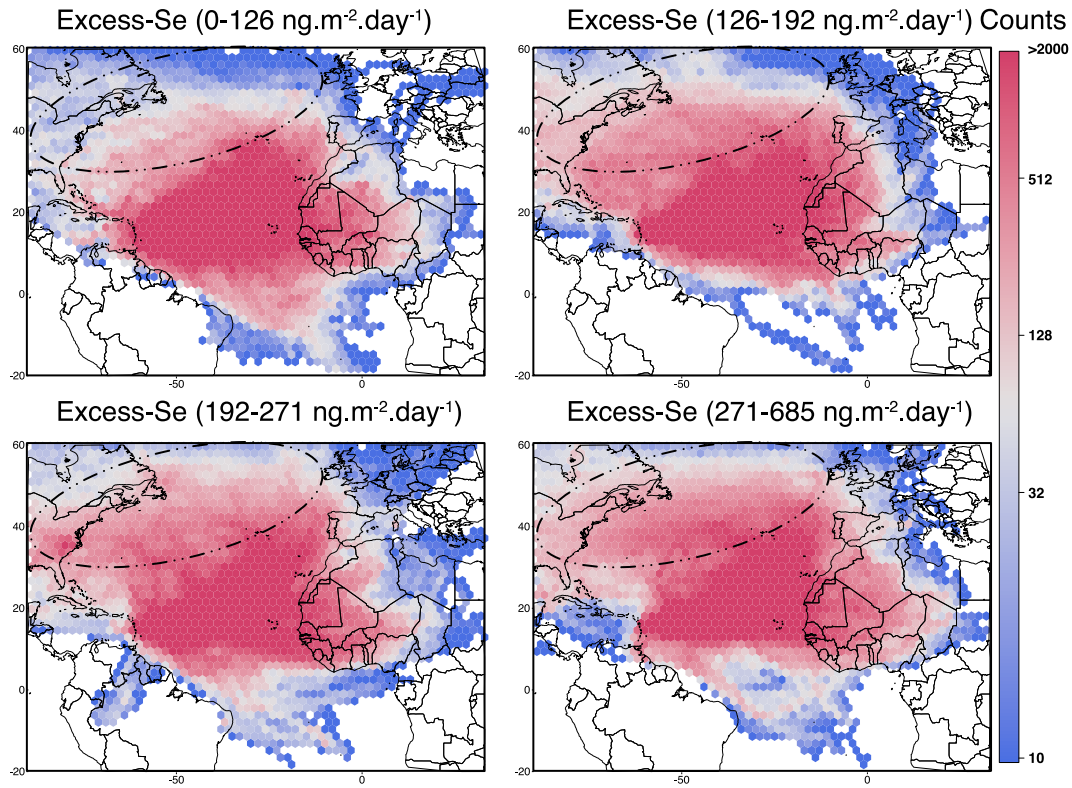

Figure A8. Gridded backward trajectory frequencies (arrival height: 1,000 m) with hexagonal binning by level of deposition flux of excess Se (in ng·m^{-2}·day^{-1}; each panel presents one quartile of data sorted by the deposition flux of excess-Se). The ellipse marks a likely source region: air masses spending longer there are more enriched in Se, Sb, and sea salt due to longer exposure to marine aerosols and anthropogenic pollution.

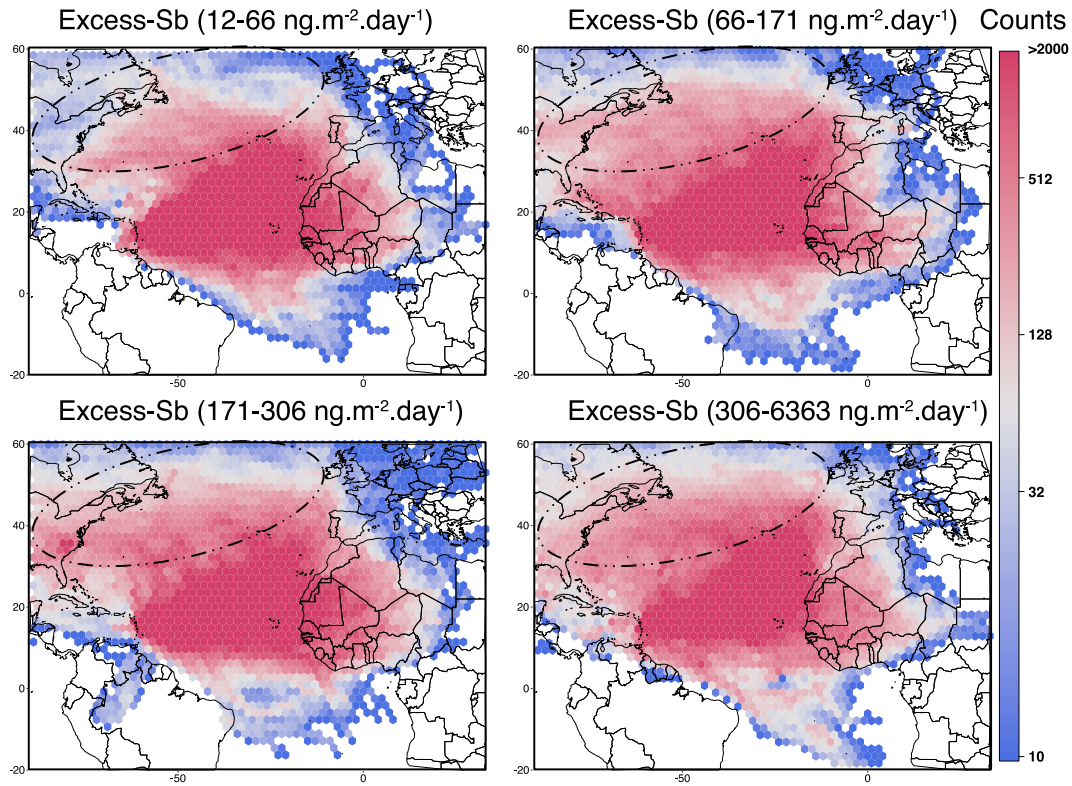

Figure A9. Gridded backward trajectory frequencies (arrival height: 1,000 m) with hexagonal binning by level of deposition flux of excess Sb (in ng·m^{-2}·day^{-1}; each panel presents one quartile of data sorted by the deposition flux of excess-Sb). The ellipse marks a likely source region: air masses spending longer there are more enriched in Se, Sb, and sea salt due to longer exposure to marine aerosols and anthropogenic pollution.

Table A2

Median Recovery Rates (RR) of Geostandard Measurements: 4 MAG-1[a] Samples, 6 SCO-1[a] Samples, SDC-1[a], STM-1[a], 3 BHVO-1[a], BE-N[b,c], LKSD-2[b,d,e,f], QLO-1[a], SLRS-4[g], SLRS-5[h,i], SLRS-6[j]

Elements	Al	Ba	Ca	Fe	K	Li	Mg	Mn
Method	AES	AES	AES	AES	Flame	AES	AES	AES
Median RR	90%	94%	93%	91%	103%	132%	94%	100%
Elements	Na	P	S	Sc	Sr	Ti	Zn	Be
Method	Flame	AES	AES	AES	AES	AES	AES	MS (LR)
Median RR	105%	109%	96%	102%	90%	86%	107%	94%
Elements	Rb	Mo	Cd	Sb	Tl	Pb	U	V
Method	MS (LR)	MS (LR)	MS (LR)	MS (LR)	MS (LR)	MS (LR)	MS (LR)	MS (MR)
Median RR	101%	83%	132%	91%	98%	87%	97%	114%
Elements	Cr	Co	Ni	Cu	As	Se	La	Ce
Method	MS (MR)	MS (MR)	MS (MR)	MS (MR)	MS (HR)	MS (HR)	MS (HR)	MS (HR)
Median RR	101%	121%	116%	100%	102%	89%	98%	102%
Elements	Pr	Nd	Sm	Eu	Gd	Tb	Dy	Ho
Method	MS (HR)	MS (HR)	MS (HR)	MS (HR)	MS (HR)	MS (HR)	MS (HR)	MS (HR)
Median RR	105%	104%	99%	95%	98%	81%	83%	80%
Elements	Er	Tm	Yb	Lu				
Method	MS (HR)	MS (HR)	MS (HR)	MS (HR)				
Median RR	80%	79%	78%	80%				

Note. Two elements, lithium (Li) and cadmium (Cd), exhibited unsatisfactory recovery rates and are therefore excluded from the main text. [a]Gladney and Roelandts (1988). [b]Govindaraju (1994). [c]Jochum et al. (2016). [d]Shaheen and Fryer (2011). [e]Hall and Pelchat (1997). [f]Leybourne et al. (2007). [g]Yeghicheyan et al. (2001). [h]Yeghicheyan et al. (2013). [i]Heimburger, Tharaud, et al. (2013). [j]Yeghicheyan et al. (2019).

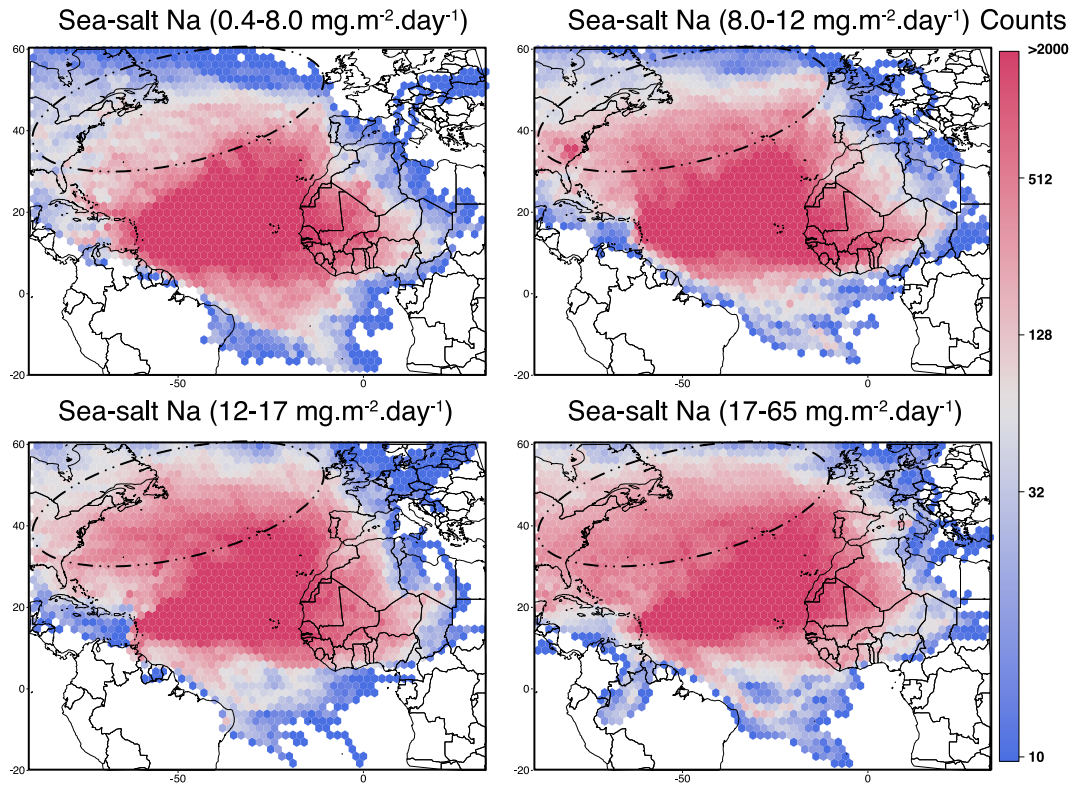

Figure A10. Gridded backward trajectory frequencies (arrival height: 1,000 m) with hexagonal binning by level of deposition flux of sea-salt Na (in $mg \cdot m^{-2} \cdot day^{-1}$; each panel presents one quartile of data sorted by the deposition flux of sea-salt Na). The ellipse marks a likely source region: air masses spending longer there are more enriched in Se, Sb, and sea salt due to longer exposure to marine aerosols and anthropogenic pollution.

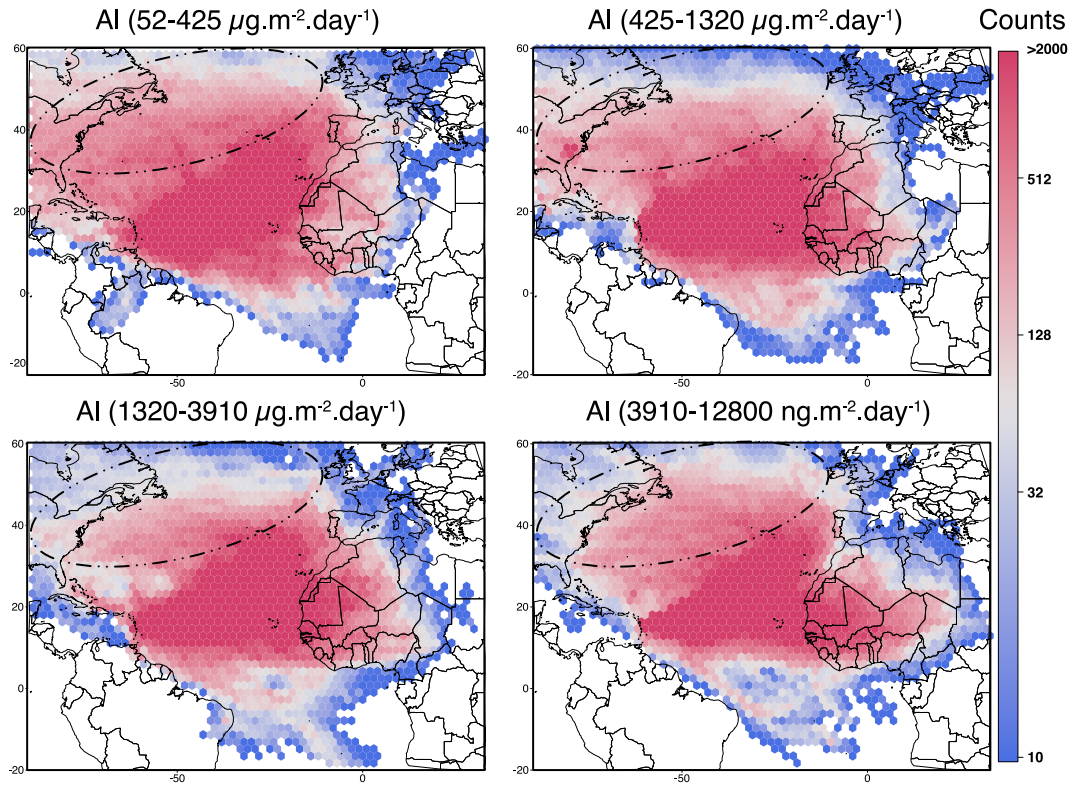

Figure A11. Gridded backward trajectory frequencies (arrival height: 1,000 m) with hexagonal binning by level of deposition flux of Al (in $\mu g \cdot m^{-2} \cdot day^{-1}$; each panel presents one quartile of data sorted by the deposition flux of Al). The ellipse marks a likely source region: air masses spending longer there are more enriched in Se, Sb, and sea salt due to longer exposure to marine aerosols and anthropogenic pollution.

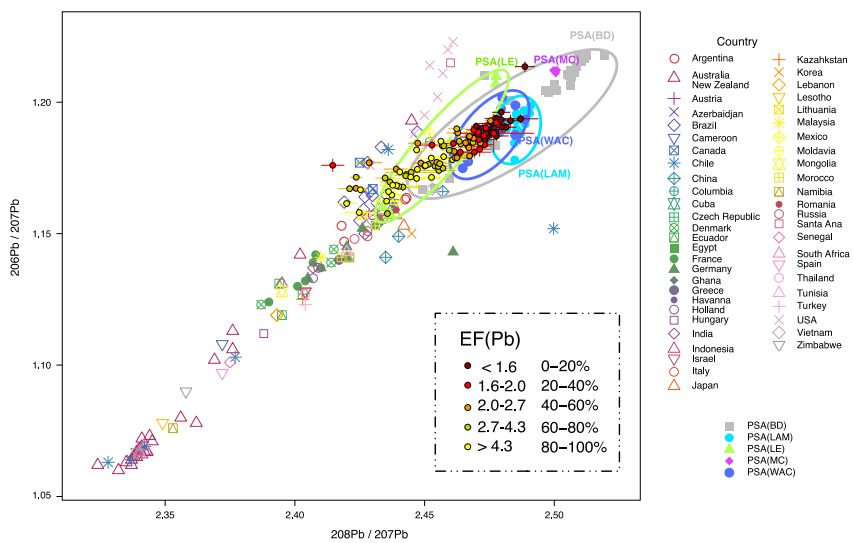

Figure A12. Pb isotopic ratios ($^{206}Pb/^{207}Pb$ vs. $^{208}Pb/^{207}Pb$) by level of Pb enrichment factor for atmospheric deposition samples. The Pb enrichment factor is represented by a color scale, and samples are separated into five levels, with 20% of the sample at each level. Yellow for high enrichment factors (corresponding to low dust deposition flux) and red for low enrichment factors (corresponding to high dust deposition flux). Error bars represent the 95% confidence interval. The PSA zone are defined from Abouchami et al. (2013); Guinoiseau et al. (2022). Anthropogenic signatures for different countries are defined from Bollhöfer and Rosman (2000, 2001).

Conflict of Interest

The authors declare no conflicts of interest relevant to this study.

Availability Statement

Data are available as Open Licence 2.0 at https://doi.org/10.18715/IPGP.2026.mm0mvo3k (Xu-Yang et al., 2026).

Acknowledgments
We thank the OVSG staff (Vincent Robert and Joanny Pierre) for their help in the field. Parts of this work (ICP-OES and HR-ICP-MS analyses) were supported by the IPGP multidisciplinary program PARI (High Resolution Analysis Platform), and by the Paris–IdF region SESAME Grant 12015908. We thank Mickael Tharaud for his help during the ICP-MS analysis, and Pascale Louvat and Julien Bouchez for their help during the organisation of Nd and Sr isotope analysis. We also thank the two anonymous reviewers for their detailed feedback and helpful comments.

References

Aarons, S., Aciego, S., & Gleason, J. (2013). Variable Hf-Sr-Nd radiogenic isotopic compositions in a Saharan dust storm over the Atlantic: Implications for dust flux to oceans, ice sheets and the terrestrial biosphere. *Chemical Geology*, *349–350*, 18–26. https://doi.org/10.1016/j.chemgeo.2013.04.010

Abouchami, W., Näthe, K., Kumar, A., Galer, S. J., Jochum, K. P., Williams, E., et al. (2013). Geochemical and isotopic characterization of the Bodélé Depression dust source and implications for transatlantic dust transport to the Amazon Basin. *Earth and Planetary Science Letters*, *380*, 112–123. https://doi.org/10.1016/j.epsl.2013.08.028

Bao, Z., Zong, C., Fang, L., Yuan, H., Chen, K., & Dai, M. (2018). Determination of Hf–Sr–Nd isotopic ratios by MC-ICP-MS using rapid acid digestion after flux-free fusion in geological materials. *Acta Geochimica*, *37*(2), 244–256. https://doi.org/10.1007/s11631-017-0207-x

Barbante, C., Schwikowski, M., Döring, T., Gäggeler, H. W., Schotterer, U., Tobler, L., et al. (2004). Historical record of European emissions of heavy metals to the atmosphere since the 1650s from Alpine snow/ice cores drilled near Monte Rosa. *Environmental Science & Technology*, *38*(15), 4085–4090. https://doi.org/10.1021/es049759r

Barkley, A. E., Pourmand, A., Longman, J., Sharifi, A., Prospero, J. M., Panechou, K., et al. (2022). Interannual variability in the source location of North African dust transported to the Amazon. *Geophysical Research Letters*, *49*(10), e2021GL097344. https://doi.org/10.1029/2021GL097344

Barkley, A. E., Prospero, J. M., Mahowald, N., Hamilton, D. S., Popendorf, K. J., Oehlert, A. M., et al. (2019). African biomass burning is a substantial source of phosphorus deposition to the Amazon, Tropical Atlantic Ocean, and Southern Ocean. *Proceedings of the National Academy of Sciences*, *116*(33), 16216–16221. https://doi.org/10.1073/pnas.1906091116

Barron, A. R., Wurzburger, N., Bellenger, J. P., Wright, S. J., Kraepiel, A. M. L., & Hedin, L. O. (2009). Molybdenum limitation of asymbiotic nitrogen fixation in tropical forest soils. *Nature Geoscience*, *2*(1), 42–45. https://doi.org/10.1038/ngeo366

Bollhöfer, A., & Rosman, K. (2000). Isotopic source signatures for atmospheric lead: The Southern Hemisphere. *Geochimica et Cosmochimica Acta*, *64*(19), 3251–3262. https://doi.org/10.1016/S0016-7037(00)00436-1

Bollhöfer, A., & Rosman, K. (2001). Isotopic source signatures for atmospheric lead: The Northern Hemisphere. *Geochimica et Cosmochimica Acta*, *65*(11), 1727–1740. https://doi.org/10.1016/S0016-7037(00)00630-X

Bozlaker, A., Prospero, J. M., Price, J., & Chellam, S. (2018). Linking Barbados mineral dust aerosols to North African sources using elemental composition and radiogenic Sr, Nd, and Pb isotope signatures. *Journal of Geophysical Research: Atmospheres*, *123*(2), 1384–1400. https://doi.org/10.1002/2017JD027505

Breuninger, E. S., Tolu, J., Aemisegger, F., Thurnherr, I., Bouchet, S., Mestrot, A., et al. (2024). Marine and terrestrial contributions to atmospheric deposition fluxes of methylated arsenic species. *Nature Communications*, *15*(1), 9623. https://doi.org/10.1038/s41467-024-53974-z

Breuninger, E. S., Tolu, J., Thurnherr, I., Aemisegger, F., Feinberg, A., Bouchet, S., et al. (2024). Influences of sources and weather dynamics on atmospheric deposition of Se species and other trace elements. *Atmospheric Chemistry and Physics*, *24*(4), 2491–2510. https://doi.org/10.5194/acp-24-2491-2024

Brewer, G. P. (1975). Minor elements in seawater. *Chemical Oceanography*, *1*, 415–496. Retrieved from https://cir.nii.ac.jp/crid/1572261549634550912

Browning, T. J., & Moore, C. M. (2023). Global analysis of ocean phytoplankton nutrient limitation reveals high prevalence of co-limitation. *Nature Communications*, *14*(1), 5014. https://doi.org/10.1038/s41467-023-40774-0

Capo, R. C., Stewart, B. W., & Chadwick, O. A. (1998). Strontium isotopes as tracers of ecosystem processes: Theory and methods. *Geoderma*, *82*(1–3), 197–225. https://doi.org/10.1016/S0016-7061(97)00102-X

Caro, G., Bourdon, B., Birck, J.-L., & Moorbath, S. (2006). High-precision $^{142}Nd/^{144}Nd$ measurements in terrestrial rocks: Constraints on the early differentiation of the Earth's mantle. *Geochimica et Cosmochimica Acta*, *70*(1), 164–191. https://doi.org/10.1016/j.gca.2005.08.015

Carslaw, D. C., & Ropkins, K. (2012). openair—An R package for air quality data analysis. *Environmental Modelling & Software*, *27–28*, 52–61. https://doi.org/10.1016/j.envsoft.2011.09.008

Cattell, F. C. R., & Scott, W. D. (1978). Copper in aerosol particles produced by the ocean. *Science*, *202*(4366), 429–430. https://doi.org/10.1126/science.202.4366.429

Chadwick, O. A., Derry, L. A., Vitousek, P. M., Huebert, B. J., & Hedin, L. O. (1999). Changing sources of nutrients during four million years of ecosystem development. *Nature*, *397*(6719), 491–497. https://doi.org/10.1038/17276

Clergue, C., Dellinger, M., Buss, H., Gaillardet, J., Benedetti, M., & Dessert, C. (2015). Influence of atmospheric deposits and secondary minerals on Li isotopes budget in a highly weathered catchment, Guadeloupe (Lesser Antilles). *Chemical Geology*, *414*, 28–41. https://doi.org/10.1016/j.chemgeo.2015.08.015

Cogez, A., Meynadier, L., Allègre, C., Limmois, D., Herman, F., & Gaillardet, J. (2015). Constraints on the role of tectonic and climate on erosion revealed by two time series analysis of marine cores around New Zealand. *Earth and Planetary Science Letters*, *410*, 174–185. https://doi.org/10.1016/j.epsl.2014.11.029

Combs, G. F. (2001). Selenium in global food systems. *British Journal of Nutrition*, *85*(5), 517–547. https://doi.org/10.1079/BJN2000280

Cutter, G. A. (1993). Metalloids in wet deposition on Bermuda: Concentrations, sources, and fluxes. *Journal of Geophysical Research*, *98*(D9), 16777–16786. https://doi.org/10.1029/93JD01689

Cutter, G. A., & Church, T. M. (1986). Selenium in western Atlantic precipitation. *Nature*, *322*(6081), 720–722. https://doi.org/10.1038/322720a0

Dessert, C., Clergue, C., Rousteau, A., Crispi, O., & Benedetti, M. F. (2020). Atmospheric contribution to cations cycling in highly weathered catchment, Guadeloupe (Lesser Antilles). *Chemical Geology*, *531*, 119354. https://doi.org/10.1016/j.chemgeo.2019.119354

Dia, A. N., Cohen, A. S., O'Nions, R. K., & Shackleton, N. J. (1992). Seawater Sr isotope variation over the past 300 kyr and influence of global climate cycles. *Nature*, *356*(6372), 786–788. https://doi.org/10.1038/356786a0

Ellam, R. (2010). The graphical presentation of lead isotope data for environmental source apportionment. *Science of the Total Environment*, *408*(16), 3490–3492. https://doi.org/10.1016/j.scitotenv.2010.03.037

Feinberg, A., Maliki, M., Stenke, A., Sudret, B., Peter, T., & Winkel, L. H. E. (2020). Mapping the drivers of uncertainty in atmospheric selenium deposition with global sensitivity analysis. *Atmospheric Chemistry and Physics*, *20*(3), 1363–1390. https://doi.org/10.5194/acp-20-1363-2020

Feinberg, A., Stenke, A., Peter, T., & Winkel, L. H. E. (2020). Constraining atmospheric selenium emissions using observations, global modeling, and Bayesian inference. *Environmental Science & Technology*, *54*(12), 7146–7155. https://doi.org/10.1021/acs.est.0c01408

Fries, D. M., James, R. H., Dessert, C., Bouchez, J., Beaumais, A., & Pearce, C. R. (2019). The response of Li and Mg isotopes to rain events in a highly-weathered catchment. *Chemical Geology*, *519*, 68–82. https://doi.org/10.1016/j.chemgeo.2019.04.023

Gladney, E. S., & Roelandts, I. (1988). 1987 Compilation of elemental concentration data for USGS BHVO-1, MAG-1, QLO-1, RGM-1, SCo-1, SDC-1, SGR-1 and STM-1. *Geostandards and Geoanalytical Research*, *12*(2), 253–362. https://doi.org/10.1111/j.1751-908X.1988.tb00053.x

Gonzalez, L., & Briottet, X. (2017). North Africa and Saudi Arabia day/night sandstorm survey (NASCube). *Remote Sensing*, *9*(9), 896. https://doi.org/10.3390/rs9090896

Govindaraju, K. (1994). 1994 compilation of working values and sample description for 383 geostandards. *Geostandards and Geoanalytical Research*, *18*(S1), 1–158. https://doi.org/10.1046/j.1365-2494.1998.53202081.x-i1

Grousset, F., Biscaye, P., Zindler, A., Prospero, J., & Chester, R. (1988). Neodymium isotopes as tracers in marine sediments and aerosols: North Atlantic. *Earth and Planetary Science Letters*, *87*(4), 367–378. https://doi.org/10.1016/0012-821X(88)90001-5

Grousset, F., & Biscaye, P. E. (2005). Tracing dust sources and transport patterns using Sr, Nd and Pb isotopes. *Chemical Geology*, *222*(3–4), 149–167. https://doi.org/10.1016/j.chemgeo.2005.05.006

Grousset, F., Parra, M., Bory, A., Martinez, P., Bertrand, P., Shimmield, G., & Ellam, R. (1998). Saharan wind regimes traced by the Sr–Nd isotopic composition of subtropical Atlantic sediments: Last glacial maximum vs today. *Quaternary Science Reviews*, *17*(4–5), 395–409. https://doi.org/10.1016/S0277-3791(97)00048-6

Guerreiro, C. V., Baumann, K.-H., Brummer, G.-J. A., Fischer, G., Korte, L. F., Merkel, U., et al. (2017). Coccolithophore fluxes in the open tropical North Atlantic: Influence of thermocline depth, Amazon water, and Saharan dust. *Biogeosciences*, *14*(20), 4577–4599. https://doi.org/10.5194/bg-14-4577-2017

Guerreiro, C. V., Ferreira, A., Cros, L., Stuut, J.-B., Baker, A., Tracana, A., et al. (2023). Response of coccolithophore communities to oceanographic and atmospheric processes across the North- and Equatorial Atlantic. *Frontiers in Marine Science*, *10*, 1119488. https://doi.org/10.3389/fmars.2023.1119488

Guinoiseau, D., Singh, S., Galer, S., Abouchami, W., Bhattacharyya, R., Kandler, K., et al. (2022). Characterization of Saharan and Sahelian dust sources based on geochemical and radiogenic isotope signatures. *Quaternary Science Reviews*, *293*, 107729. https://doi.org/10.1016/j.quascirev.2022.107729

Hall, G. E., & Pelchat, J. (1997). [1]Determination of As, Bi, Sb, Se and Te in fifty five reference materials by hydride generation ICP-MS. *Geostandards Newsletter*, *21*(1), 85–91. https://doi.org/10.1111/j.1751-908X.1997.tb00534.x

Heartsill-Scalley, T., Scatena, F., Estrada, C., McDowell, W., & Lugo, A. (2007). Disturbance and long-term patterns of rainfall and throughfall nutrient fluxes in a subtropical wet forest in Puerto Rico. *Journal of Hydrology*, *333*(2–4), 472–485. https://doi.org/10.1016/j.jhydrol.2006.09.019

Heimburger, A., Losno, R., & Triquet, S. (2013). Solubility of iron and other trace elements in rainwater collected on the Kerguelen Islands (South Indian Ocean). *Biogeosciences*, *10*(10), 6617–6628. https://doi.org/10.5194/bg-10-6617-2013

Heimburger, A., Losno, R., Triquet, S., Dulac, F., & Mahowald, N. (2012). Direct measurements of atmospheric iron, cobalt, and aluminum-derived dust deposition at Kerguelen Islands. *Global Biogeochemical Cycles*, *26*(4), GB4016. https://doi.org/10.1029/2012GB004301

Heimburger, A., Tharaud, M., Monna, F., Losno, R., Desboeufs, K., & Nguyen, E. B. (2013). SLRS-5 elemental concentrations of thirty-three uncertified elements deduced from SLRS-5/SLRS-4 ratios. *Geostandards and Geoanalytical Research*, *37*(1), 77–85. https://doi.org/10.1111/j.1751-908X.2012.00185.x

Hudson-Edwards, K. A., Bristow, C. S., Cibin, G., Mason, G., & Peacock, C. L. (2014). Solid-phase phosphorus speciation in Saharan Bodélé Depression dusts and source sediments. *Chemical Geology*, *384*, 16–26. https://doi.org/10.1016/j.chemgeo.2014.06.014

Hur, S. D., Soyol-Erdene, T., Hwang, H. J., Han, C., Gabrielli, P., Barbante, C., et al. (2013). Climate-related variations in atmospheric Sb and Tl in the EPICA Dome C ice (East Antarctica) during the past 800,000 years. *Global Biogeochemical Cycles*, *27*(3), 930–940. https://doi.org/10.1002/gbc.20079

IPCC. (2023). *Climate Change 2021—The Physical Science Basis: Working Group I Contribution to the Sixth Assessment Report of the Intergovernmental Panel on Climate Change* (1st ed.). Cambridge University Press. https://doi.org/10.1017/9781009157896

Izquierdo, R., & Avila, A. (2012). Comparison of collection methods to determine atmospheric deposition in a rural Mediterranean site (NE Spain). *Journal of Atmospheric Chemistry*, *69*(4), 351–368. https://doi.org/10.1007/s10874-012-9246-1

Jacobsen, S., & Wasserburg, G. (1984). Sm-Nd isotopic evolution of chondrites and achondrites, II. *Earth and Planetary Science Letters*, *67*(2), 137–150. https://doi.org/10.1016/0012-821X(84)90109-2

Jewell, A. M., Drake, N., Crocker, A. J., Bakker, N. L., Kunkelova, T., Bristow, C. S., et al. (2021). Three North African dust source areas and their geochemical fingerprint. *Earth and Planetary Science Letters*, *554*, 116645. https://doi.org/10.1016/j.epsl.2020.116645

Jiang, J., Wu, Y., Sun, G., Zhang, L., Li, Z., Sommar, J., et al. (2021). Characteristics, accumulation, and potential health risks of antimony in atmospheric particulate matter. *ACS Omega*, *6*(14), 9460–9470. https://doi.org/10.1021/acsomega.0c06091

Jickells, T. D., An, Z. S., Andersen, K. K., Baker, A. R., Bergametti, G., Brooks, N., et al. (2005). Global iron connections between desert dust, ocean biogeochemistry, and climate. *Science*, *308*(5718), 67–71. https://doi.org/10.1126/science.1105959

Jochum, K. P., Weis, U., Schwager, B., Stoll, B., Wilson, S. A., Haug, G. H., et al. (2016). Reference values following ISO guidelines for frequently requested rock reference materials. *Geostandards and Geoanalytical Research*, *40*(3), 333–350. https://doi.org/10.1111/j.1751-908X.2015.00392.x

Kadko, D., Landing, W. M., & Buck, C. S. (2020). Quantifying atmospheric trace element deposition over the ocean on a global scale with satellite rainfall products. *Geophysical Research Letters*, *47*(7), e2019GL086357. https://doi.org/10.1029/2019GL086357

Komárek, M., Ettler, V., Chrastný, V., & Mihaljevič, M. (2008). Lead isotopes in environmental sciences: A review. *Environment International*, *34*(4), 562–577. https://doi.org/10.1016/j.envint.2007.10.005

Krachler, M., Zheng, J., Fisher, D., & Shotyk, W. (2008). Atmospheric Sb in the Arctic during the past 16,000 years: Responses to climate change and human impacts. *Global Biogeochemical Cycles*, *22*(1), 2007GB002998. https://doi.org/10.1029/2007GB002998

Krachler, M., Zheng, J., Koerner, R., Zdanowicz, C., Fisher, D., & Shotyk, W. (2005). Increasing atmospheric antimony contamination in the northern hemisphere: Snow and ice evidence from Devon Island, Arctic Canada. *Journal of Environmental Monitoring*, *7*(12), 1169. https://doi.org/10.1039/b509373b

Kumar, A., Abouchami, W., Galer, S., Garrison, V., Williams, E., & Andreae, M. (2014). A radiogenic isotope tracer study of transatlantic dust transport from Africa to the Caribbean. *Atmospheric Environment*, *82*, 130–143. https://doi.org/10.1016/j.atmosenv.2013.10.021

Kumar, A., Abouchami, W., Galer, S., Singh, S. P., Fomba, K., Prospero, J., & Andreae, M. (2018). Seasonal radiogenic isotopic variability of the African dust outflow to the tropical Atlantic Ocean and across to the Caribbean. *Earth and Planetary Science Letters*, *487*, 94–105. https://doi.org/10.1016/j.epsl.2018.01.025

Landing, W. M., Caffrey, J. M., Nolek, S. D., Gosnell, K. J., & Parker, W. C. (2010). Atmospheric wet deposition of Mercury and other trace elements in Pensacola, Florida. *Atmospheric Chemistry and Physics*, *10*(10), 4867–4877. https://doi.org/10.5194/acp-10-4867-2010

Langner, P., Mikutta, C., & Kretzschmar, R. (2012). Arsenic sequestration by organic sulphur in peat. *Nature Geoscience*, *5*(1), 66–73. https://doi.org/10.1038/ngeo1329

Lawrence, C. R., & Neff, J. C. (2009). The contemporary physical and chemical flux of aeolian dust: A synthesis of direct measurements of dust deposition. *Chemical Geology*, *267*(1–2), 46–63. https://doi.org/10.1016/j.chemgeo.2009.02.005

Leybourne, M. I., Denison, R. E., Cousens, B. L., Bezys, R. K., Gregoire, D. C., Boyle, D. R., & Dobrzanski, E. (2007). Geochemistry, geology, and isotopic (Sr, S, and B) composition of evaporites in the Lake St. Martin impact structure: New constraints on the age of melt rock formation. *Geochemistry, Geophysics, Geosystems*, *8*(3), 2006GC001481. https://doi.org/10.1029/2006GC001481

Lu, L., Li, L., Rathod, S., Hess, P., Martínez, C., Fernandez, N., et al. (2024). Characterizing the atmospheric Mn cycle and its impact on terrestrial biogeochemistry. *Global Biogeochemical Cycles*, *38*(4), e2023GB007967. https://doi.org/10.1029/2023GB007967

Mahowald, N., Albani, S., Kok, J. F., Engelstaeder, S., Scanza, R., Ward, D. S., & Flanner, M. G. (2014). The size distribution of desert dust aerosols and its impact on the Earth system. *Aeolian Research*, *15*, 53–71. https://doi.org/10.1016/j.aeolia.2013.09.002

Mahowald, N., Li, L., Vira, J., Prank, M., Hamilton, D. S., Matsui, H., et al. (2025). AERO-MAP: A data compilation and modeling approach to understand spatial variability in fine- and coarse-mode aerosol composition. *Atmospheric Chemistry and Physics*, *25*(9), 4665–4702. https://doi.org/10.5194/acp-25-4665-2025

Mahowald, N., Ward, D. S., Kloster, S., Flanner, M. G., Heald, C. L., Heavens, N. G., et al. (2011). Aerosol impacts on climate and biogeochemistry. *Annual Review of Environment and Resources*, *36*(1), 45–74. https://doi.org/10.1146/annurev-environ-042009-094507

Mao, J., Zhou, L., Wu, L., Chen, W., Wang, X., & Yu, P. (2021). Evaluation of biogenic organic aerosols in the Amazon rainforest using WRF-Chem with MOSAIC. *Journal of Geophysical Research: Atmospheres*, *126*(23), e2021JD034913. https://doi.org/10.1029/2021JD034913

Marsay, C. M., Landing, W. M., Umstead, D., Till, C. P., Freiberger, R., Fitzsimmons, J. N., et al. (2022). Does sea spray aerosol contribute significantly to aerosol trace element loading? A case study from the U.S. GEOTRACES Pacific Meridional transect (GP15). *Global Biogeochemical Cycles*, *36*(8), e2022GB007416. https://doi.org/10.1029/2022GB007416

Martin, S. T., Andreae, M. O., Artaxo, P., Baumgardner, D., Chen, Q., Goldstein, A. H., et al. (2010). Sources and properties of Amazonian aerosol particles. *Reviews of Geophysics*, *48*(2), RG2002. https://doi.org/10.1029/2008RG000280

McClintock, M., Brocard, G., Willenbring, J., Tamayo, C., Porder, S., & Pett-Ridge, J. (2015). Spatial variability of African dust in soils in a montane tropical landscape in Puerto Rico. *Chemical Geology*, *412*, 69–81. https://doi.org/10.1016/j.chemgeo.2015.06.032

McClintock, M., McDowell, W., González, G., Schulz, M., & Pett-Ridge, J. (2019). African dust deposition in Puerto Rico: Analysis of a 20-year rainfall chemistry record and comparison with models. *Atmospheric Environment*, *216*, 116907. https://doi.org/10.1016/j.atmosenv.2019.116907

Monna, F., Bouchaou, L., Rambeau, C., Losno, R., Bruguier, O., Dongarrà, G., et al. (2012). Lichens used as monitors of atmospheric pollution around Agadir (southwestern Morocco)—A case study predating lead-free gasoline. *Water, Air, & Soil Pollution*, *223*(3), 1263–1274. https://doi.org/10.1007/s11270-011-0942-2

Moore, C. M., Mills, M. M., Arrigo, K. R., Berman-Frank, I., Bopp, L., Boyd, P. W., et al. (2013). Processes and patterns of oceanic nutrient limitation. *Nature Geoscience*, *6*(9), 701–710. https://doi.org/10.1038/ngeo1765

Moreno, T., Querol, X., Castillo, S., Alastuey, A., Cuevas, E., Herrmann, L., et al. (2006). Geochemical variations in aeolian mineral particles from the Sahara–Sahel Dust Corridor. *Chemosphere*, *65*(2), 261–270. https://doi.org/10.1016/j.chemosphere.2006.02.052

Morera-Gómez, Y., Santamaría, J. M., Elustondo, D., Lasheras, E., & Alonso-Hernández, C. M. (2019). Determination and source apportionment of major and trace elements in atmospheric bulk deposition in a Caribbean rural area. *Atmospheric Environment*, *202*, 93–104. https://doi.org/10.1016/j.atmosenv.2019.01.019

Munroe, J. S., Norris, E. D., Carling, G. T., Beard, B. L., Satkoski, A. M., & Liu, L. (2019). Isotope fingerprinting reveals western North American sources of modern dust in the Uinta Mountains, Utah, USA. *Aeolian Research*, *38*, 39–47. https://doi.org/10.1016/j.aeolia.2019.03.005

Nagender Nath, B., Makishima, A., Noordmann, J., Tanaka, R., & Nakamura, E. (2009). Comprehensive analysis for major, minor and trace element contents and Sr-Nd-Pb-Hf isotope ratios in sediment reference materials, JSd-1 and MAG-1. *Geochemical Journal*, *43*(3), 207–216. https://doi.org/10.2343/geochemj.1.0018

Okin, G. S., Baker, A. R., Tegen, I., Mahowald, N. M., Dentener, F. J., Duce, R. A., et al. (2011). Impacts of atmospheric nutrient deposition on marine productivity: Roles of nitrogen, phosphorus, and iron. *Global Biogeochemical Cycles*, *25*(2), GB2022. https://doi.org/10.1029/2010GB003858

Pabortsava, K., Lampitt, R. S., Benson, J., Crowe, C., McLachlan, R., Le Moigne, F. A. C., et al. (2017). Carbon sequestration in the deep Atlantic enhanced by Saharan dust. *Nature Geoscience*, *10*(3), 189–194. https://doi.org/10.1038/ngeo2899

Pacyna, J. M., & Pacyna, E. G. (2001). An assessment of global and regional emissions of trace metals to the atmosphere from anthropogenic sources worldwide. *Environmental Reviews*, *9*(4), 269–298. https://doi.org/10.1139/a01-012

Paoletti, F., Sirini, P., Seifert, H., & Vehlow, J. (2001). Fate of antimony in municipal solid waste incineration. *Chemosphere*, *42*(5–7), 533–543. https://doi.org/10.1016/S0045-6535(00)00225-3

Pavageau, M.-P., Pécheyran, C., Krupp, E. M., Morin, A., & Donard, O. F. X. (2002). Volatile metal species in coal combustion flue gas. *Environmental Science & Technology*, *36*(7), 1561–1573. https://doi.org/10.1021/es015595s

Pett-Ridge, J. C., Derry, L. A., & Barrows, J. K. (2009). Ca/Sr and $^{87}Sr/^{86}Sr$ ratios as tracers of Ca and Sr cycling in the Rio Icacos watershed, Luquillo Mountains, Puerto Rico. *Chemical Geology*, *267*(1–2), 32–45. https://doi.org/10.1016/j.chemgeo.2008.11.022

Pourmand, A., Prospero, J. M., & Sharifi, A. (2014). Geochemical fingerprinting of trans-Atlantic African dust based on radiogenic Sr-Nd-Hf isotopes and rare earth element anomalies. *Geology*, *42*(8), 675–678. https://doi.org/10.1130/G35624.1

Prospero, J. M., Collard, F.-X., Molinié, J., & Jeannot, A. (2014). Characterizing the annual cycle of African dust transport to the Caribbean Basin and South America and its impact on the environment and air quality: African dust transport to South America. *Global Biogeochemical Cycles*, *28*(7), 757–773. https://doi.org/10.1002/2013GB004802

Prospero, J. M., Landing, W. M., & Schulz, M. (2010). African dust deposition to Florida: Temporal and spatial variability and comparisons to models. *Journal of Geophysical Research*, *115*(D13), D13304. https://doi.org/10.1029/2009JD012773

R Core Team. (2018). *R: A Language and Environment for Statistical Computing*. R Foundation for Statistical Computing. Retrieved from http://www.R-project.org/

Rahn, K. A. (1976). The chemical composition of the atmospheric aerosol. Retrieved from https://books.google.fr/books?hl=fr&lr=&id=q-dOAQAAMAAJ&oi=fnd&pg=PA1&dq=The+Chemical+Composition+of+the+Atmospheric+Aerosol&ots=Gz11fOEivU&sig=lYh8sJjlLtUuA5KXxST6YbXU34c#v=onepage&q=The%20Chemical%20Composition%20of%20the%20Atmospheric%20Aerosol&f=false

Rathod, S. D., Hamilton, D. S., Mahowald, N. M., Klimont, Z., Corbett, J. J., & Bond, T. C. (2020). A mineralogy-based anthropogenic combustion-iron emission inventory. *Journal of Geophysical Research: Atmospheres*, *125*(17), e2019JD032114. https://doi.org/10.1029/2019JD032114

Rathod, S. D., Hamilton, D. S., Nino, L., Kreidenweis, S. M., Bian, Q., Mahowald, N. M., et al. (2024). Constraining present-day anthropogenic total iron emissions using model and observations. *Journal of Geophysical Research: Atmospheres*, *129*(17), e2023JD040332. https://doi.org/10.1029/2023JD040332

R Core Team. (2021). *R: A Language and Environment for Statistical Computing*. R Foundation for Statistical Computing. Retrieved from https://www.R-project.org/

Ridley, D. A., Heald, C. L., & Ford, B. (2012). North African dust export and deposition: A satellite and model perspective. *Journal of Geophysical Research*, *117*(D2), 2011JD016794. https://doi.org/10.1029/2011JD016794

Rousk, K., Degboe, J., Michelsen, A., Bradley, R., & Bellenger, J. (2017). Molybdenum and phosphorus limitation of moss-associated nitrogen fixation in boreal ecosystems. *New Phytologist*, *214*(1), 97–107. https://doi.org/10.1111/nph.14331

Rousseau, D.-D., Chauvel, C., Hopcroft, P., Gutiérrez, P., Saulnier-Copard, S., Antoine, P., et al. (2025). A remote input of African dust to Last Glacial Europe. https://doi.org/10.5194/egusphere-egu25-3549

Rudnick, R., & Gao, S. (2014). Composition of the continental crust. In *Treatise on geochemistry* (pp. 1–51). Elsevier. https://doi.org/10.1016/B978-0-08-095975-7.00301-6

Scheuvens, D., Schütz, L., Kandler, K., Ebert, M., & Weinbruch, S. (2013). Bulk composition of northern African dust and its source sediments—A compilation. *Earth-Science Reviews*, *116*, 170–194. https://doi.org/10.1016/j.earscirev.2012.08.005

Schlesinger, W. H., Klein, E. M., & Vengosh, A. (2022). The global biogeochemical cycle of arsenic. *Global Biogeochemical Cycles*, *36*(11), e2022GB007515. https://doi.org/10.1029/2022GB007515

Schlosser, C., Klar, J. K., Wake, B. D., Snow, J. T., Honey, D. J., Woodward, E. M. S., et al. (2014). Seasonal ITCZ migration dynamically controls the location of the (sub)tropical Atlantic biogeochemical divide. *Proceedings of the National Academy of Sciences*, *111*(4), 1438–1442. https://doi.org/10.1073/pnas.1318670111

Shaheen, M. E., & Fryer, B. J. (2011). A simple solution to expanding available reference materials for Laser Ablation Inductively Coupled Plasma Mass Spectrometry analysis: Applications to sedimentary materials. *Spectrochimica Acta Part B: Atomic Spectroscopy*, *66*(8), 627–636. https://doi.org/10.1016/j.sab.2011.06.010

Skonieczny, C., Bory, A., Bout-Roumazeilles, V., Abouchami, W., Galer, S., Crosta, X., et al. (2013). A three-year time series of mineral dust deposits on the West African margin: Sedimentological and geochemical signatures and implications for interpretation of marine paleo-dust records. *Earth and Planetary Science Letters*, *364*, 145–156. https://doi.org/10.1016/j.epsl.2012.12.039

Skonieczny, C., Bory, A., Bout-Roumazeilles, V., Abouchami, W., Galer, S. J. G., Crosta, X., et al. (2011). The 7–13 March 2006 major Saharan outbreak: Multiproxy characterization of mineral dust deposited on the West African margin. *Journal of Geophysical Research*, *116*(D18), D18210. https://doi.org/10.1029/2011JD016173

Smichowski, P. (2008). Antimony in the environment as a global pollutant: A review on analytical methodologies for its determination in atmospheric aerosols. *Talanta*, *75*(1), 2–14. https://doi.org/10.1016/j.talanta.2007.11.005

Stefels, J., Steinke, M., Turner, S., Malin, G., & Belviso, S. (2007). Environmental constraints on the production and removal of the climatically active gas dimethylsulphide (DMS) and implications for ecosystem modelling. *Biogeochemistry*, *83*(1–3), 245–275. https://doi.org/10.1007/s10533-007-9091-5

Stein, A. F., Draxler, R. R., Rolph, G. D., Stunder, B. J. B., Cohen, M. D., & Ngan, F. (2015). NOAA's HYSPLIT atmospheric transport and dispersion modeling system. *Bulletin of the American Meteorological Society*, *96*(12), 2059–2077. https://doi.org/10.1175/BAMS-D-14-00110.1

Stewart, B. W., Capo, R. C., & Chadwick, O. A. (1998). Quantitative strontium isotope models for weathering, pedogenesis and biogeochemical cycling. *Geoderma*, *82*(1–3), 173–195. https://doi.org/10.1016/S0016-7061(97)00101-8

Suárez, M. H., Molina Pérez, D., Rodríguez-Rodríguez, E., Díaz Romero, C., Espinosa Borreguero, F., & Galindo-Villardón, P. (2016). The compositional HJ-biplot—A new approach to identifying the links among bioactive compounds of tomatoes. *International Journal of Molecular Sciences*, *17*(11), 1828. https://doi.org/10.3390/ijms17111828

van den Boogaart, K. G., & Tolosana-Delgado, R. (2013). *Analyzing compositional data with R*. Springer Berlin Heidelberg. https://doi.org/10.1007/978-3-642-36809-7

Van Der Does, M., Pourmand, A., Sharifi, A., & Stuut, J.-B. W. (2018). North African mineral dust across the tropical Atlantic Ocean: Insights from dust particle size, radiogenic Sr-Nd-Hf isotopes and rare earth elements (REE). *Aeolian Research*, *33*, 106–116. https://doi.org/10.1016/j.aeolia.2018.06.001

Van Der Jagt, H., Friese, C., Stuut, J. W., Fischer, G., & Iversen, M. H. (2018). The ballasting effect of Saharan dust deposition on aggregate dynamics and carbon export: Aggregation, settling, and scavenging potential of marine snow. *Limnology and Oceanography*, *63*(3), 1386–1394. https://doi.org/10.1002/lno.10779

Van De Velde, K., Ferrari, C., Barbante, C., Moret, I., Bellomi, T., Hong, S., & Boutron, C. (1999). A 200 year record of atmospheric cobalt, chromium, molybdenum, and antimony in high altitude alpine firn and ice. *Environmental Science & Technology*, *33*(20), 3495–3501. https://doi.org/10.1021/es990066y

Vet, R., Artz, R. S., Carou, S., Shaw, M., Ro, C.-U., Aas, W., et al. (2014). A global assessment of precipitation chemistry and deposition of sulfur, nitrogen, sea salt, base cations, organic acids, acidity and pH, and phosphorus. *Atmospheric Environment*, *93*, 3–100. https://doi.org/10.1016/j.atmosenv.2013.10.060

Violaki, K., Panagiotopoulos, C., Avalos, C. E., Rossi, P., Abboud, E., Kanakidou, M., & Nenes, A. (2025). Solid-state 31P NMR reveals the biological organophosphorus compounds as the dominant phosphorus species in Saharan dust aerosols. *Communications Earth & Environment*, *6*(1), 225. https://doi.org/10.1038/s43247-025-02164-w

Vriens, B., Lenz, M., Charlet, L., Berg, M., & Winkel, L. H. (2014). Natural wetland emissions of methylated trace elements. *Nature Communications*, *5*(1), 3035. https://doi.org/10.1038/ncomms4035

Washington, R., & Todd, M. C. (2005). Atmospheric controls on mineral dust emission from the Bodélé Depression, Chad: The role of the low level jet. *Geophysical Research Letters*, *32*(17), L17701. https://doi.org/10.1029/2005GL023597

Weis, D., Kieffer, B., Maerschalk, C., Barling, J., De Jong, J., Williams, G. A., et al. (2006). High-precision isotopic characterization of USGS reference materials by TIMS and MC-ICP-MS. *Geochemistry, Geophysics, Geosystems*, *7*(8), 2006GC001283. https://doi.org/10.1029/2006GC001283

Weis, D., Kieffer, B., Maerschalk, C., Pretorius, W., & Barling, J. (2005). High-precision Pb-Sr-Nd-Hf isotopic characterization of USGS BHVO-1 and BHVO-2 reference materials. *Geochemistry, Geophysics, Geosystems*, *6*(2), 2004GC000852. https://doi.org/10.1029/2004GC000852

Weisel, C. P., Duce, R. A., Fasching, J. L., & Heaton, R. W. (1984). Estimates of the transport of trace metals from the ocean to the atmosphere. *Journal of Geophysical Research*, *89*(D7), 11607–11618. https://doi.org/10.1029/JD089iD07p11607

Whipkey, C., Capo, R., Chadwick, O., & Stewart, B. (2000). The importance of sea spray to the cation budget of a coastal Hawaiian soil: A strontium isotope approach. *Chemical Geology*, *168*(1–2), 37–48. https://doi.org/10.1016/S0009-2541(00)00187-X

Witt, M., Baker, A., & Jickells, T. (2006). Atmospheric trace metals over the Atlantic and South Indian Oceans: Investigation of metal concentrations and lead isotope ratios in coastal and remote marine aerosols. *Atmospheric Environment*, *40*(28), 5435–5451. https://doi.org/10.1016/j.atmosenv.2006.04.041

Wong, M. Y., Rathod, S. D., Marino, R., Li, L., Howarth, R. W., Alastuey, A., et al. (2021). Anthropogenic perturbations to the atmospheric molybdenum cycle. *Global Biogeochemical Cycles*, *35*(2), e2020GB006787. https://doi.org/10.1029/2020GB006787

Wurzburger, N., Bellenger, J. P., Kraepiel, A. M. L., & Hedin, L. O. (2012). Molybdenum and phosphorus interact to constrain asymbiotic nitrogen fixation in tropical forests. *PLoS One*, *7*(3), e33710. https://doi.org/10.1371/journal.pone.0033710

Xu-Yang, Y., Dessert, C., & Losno, R. (2022). Atmospheric deposition over the Caribbean region: Sea salt and Saharan dust are sources of essential elements on the Island of Guadeloupe. *Journal of Geophysical Research: Atmospheres*, *127*(22), e2022JD037175. https://doi.org/10.1029/2022JD037175

Xu-Yang, Y., Losno, R., Dessert, C., Cogez, A., Tharaud, M., & Louvat, P. (2026). Trace elements in total atmospheric deposition directly measured over the Caribbean region: Natural versus anthropogenic sources and geographic origin [Dataset]. *IPGP Research Collection*. https://doi.org/10.18715/IPGP.2026.mm0mvo3k

Xu-Yang, Y., Losno, R., Dessert, C., Monna, F., Mahowald, N. M., & Tharaud, M. (2025). Atmospheric aerosols versus total atmospheric deposition in Guadeloupe (Lesser Antilles): Composition, concentration, and flux. *Journal of Geophysical Research: Atmospheres*, *130*(7), e2024JD042682. https://doi.org/10.1029/2024JD042682

Xu-Yang, Y., Losno, R., Monna, F., Rajot, J.-L., Labiadh, M., Bergametti, G., & Marticorena, B. (2021). Compositional data analysis (CoDA) as a tool to evaluate a new low-cost settling-based PM_{10} sampling head in a desert dust source region. *Atmospheric Measurement Techniques*, *14*(12), 7657–7680. https://doi.org/10.5194/amt-2021-70

Yeghicheyan, D., Aubert, D., Bouhnik-Le Coz, M., Chmeleff, J., Delpoux, S., Djouraev, I., et al. (2019). A new interlaboratory characterisation of silicon, rare earth elements and twenty-two other trace element mass fractions in the natural river water certified reference material SLRS-6 (NRC-CNRC). *Geostandards and Geoanalytical Research*, *43*(3), 475–496. https://doi.org/10.1111/ggr.12268

Yeghicheyan, D., Bossy, C., Bouhnik Le Coz, M., Douchet, C., Granier, G., Heimburger, A., et al. (2013). A compilation of silicon, rare earth element and twenty-one other trace element concentrations in the natural river water reference material SLRS-5 (NRC-CNRC). *Geostandards and Geoanalytical Research*, *37*(4), 449–467. https://doi.org/10.1111/j.1751-908X.2013.00232.x

Yeghicheyan, D., Carignan, J., Valladon, M., Coz, M. B., Cornec, F. L., Castrec-Rouelle, M., et al. (2001). A compilation of silicon and thirty one trace elements measured in the natural river water reference material SLRS-4 (NRC-CNRC). *Geostandards and Geoanalytical Research*, *25*(2–3), 465–474. https://doi.org/10.1111/j.1751-908X.2001.tb00617.x

Yu, H., Chin, M., Yuan, T., Bian, H., Remer, L. A., Prospero, J. M., et al. (2015). The fertilizing role of African dust in the Amazon rainforest: A first multiyear assessment based on data from Cloud-Aerosol LiDAR and Infrared Pathfinder Satellite Observations: Dust deposition in the Amazon Rainforest. *Geophysical Research Letters*, *42*(6), 1984–1991. https://doi.org/10.1002/2015GL063040

Yu, Y., Kalashnikova, O. V., Garay, M. J., Lee, H., Notaro, M., Campbell, J. R., et al. (2020). Disproving the Bodélé depression as the primary source of dust fertilizing the Amazon Rainforest. *Geophysical Research Letters*, *47*(13), e2020GL088020. https://doi.org/10.1029/2020GL088020

Zhao, W., Balsam, W., Williams, E., Long, X., & Ji, J. (2018). Sr–Nd–Hf isotopic fingerprinting of transatlantic dust derived from North Africa. *Earth and Planetary Science Letters*, *486*, 23–31. https://doi.org/10.1016/j.epsl.2018.01.004

Zhou, S., Salter, M., Bertram, T., Azevedo, E. B., Reis, F., & Wang, J. (2025). Shoreline wave breaking strongly enhances the coastal sea spray aerosol population: Climate and air quality implications. *Science Advances*, *11*(35), eadw0343.